https://doi.org/10.5194/se-2019-163
Preprint. Discussion started: 4 November 2019

Solid Earth Discussions

Sediment history mirrors Pleistocene aridification in the Gobi Desert (Ejina Basin, NW China)

Georg Schwamborn[1,2], Kai Hartmann[1], Bernd Wünnemann[1,3], Wolfgang Rösler[4], Annette Wefer-Roehl[5], Jörg Pross[6], Bernhard Diekmann[2]

[1]Freie Universität Berlin, Applied Physical Geography, 12249 Berlin, Germany
[2]Alfred Wegener Institute, Helmholtz Centre for Polar and Marine Research, 14473 Potsdam, Germany
[3]East China Normal University, State Key Laboratory of Estuarine and Coastal Research, Shanghai 200241, China
[4]University of Tuebingen, Department of Geosciences, 72074 Tuebingen, Germany
[5]Senckenberg Gesellschaft für Naturforschung, 60325 Frankfurt, Germany
[6]Institute of Earth Sciences, Heidelberg University, 69120 Heidelberg, Germany

Correspondence to: Georg Schwamborn (georg.schwamborn@fu-berlin.de)

Abstract. Central Asia is a large-scale source of dust transport, but also holds a prominent changing hydrological system during the Quaternary. A 223-m-long sediment core (GN200) was recovered from the Ejina Basin (synonymously Gaxun Nur Basin) in NW China to reconstructing the main transitional modes of water availability in the area during the Quaternary. The core has been drilled from the Heihe alluvial fan, one of the world's largest continental alluvial fan, which covers a part of the Gobi Desert. Grain-size distributions supported by endmember modelling analyses, geochemical-mineralogical compositions (based on XRF and XRD measurements), and bioindicator data (ostracods, gastropods, n-alkanes with leaf-wax δD) are used to infer the main transport processes and related environmental changes during the Pleistocene. Magnetostratigraphy supported by radionuclide dating provides the age model. Grain-size endmembers indicate that lake, playa (sheetflood), fluvial, and aeolian dynamics are the major factors influencing sedimentation in the Ejina Basin. Core GN200 reached the Pre-Quaternary quartz- and plagioclase-rich 'Red Clay Formation' and reworked material derived from it in the core bottom. This part is overlain by silt-dominated sediments between 217 and 110 m core depth, which represent a period of lacustrine and playa-lacustrine sedimentation that presumably formed within an endorheic basin. The upper core half between 110 and 0 m is composed of mainly silty to sandy sediments derived from the Heihe River that have accumulated in a giant sediment fan until modern time. Apart from the transition from a siltier to a sandier environment with frequent switches between sediment types upcore, the clay mineral fraction is indicative for different environments. Mixed layer clay minerals (chlorite/smectite) are increased in the basal 'Red Clay Formation' and reworked sediments, smectite is indicative for lacustrine-playa deposits, and an increased chlorite content is characteristic of the Heihe river deposits. The sediment succession in core GN200 based on the detrital proxy interpretation demonstrates that lake-playa sedimentation in the Ejina Basin has been disrupted likely due to tectonic events in the southern part of the catchment around 1 Ma BP. At this time Heihe river broke through from the Hexi Corridor through the Heli Shan ridge into the northern Ejina Basin. This initiated the alluvial fan progradation into the Ejina Basin. Presently the sediment bulge repels the diminishing lacustrine environment further north. In this sense, the uplift of the hinterland served as a tipping element that triggered landscape transformation in the Northern Tibetan foreland (i.e., the Hexi

https://doi.org/10.5194/se-2019-163
Preprint. Discussion started: 4 November 2019

Corridor) and further on in the adjacent northern intracontinental Ejina Basin. The onset of alluvial fan formation coincides with increased sedimentation rates on the Chinese loess plateau, suggesting that the Heihe fluvial/alluvial fan may have served as a prominent upwind sediment source for it.

1 Introduction

The aridification of the Asian interior since ~2.95-2.5 Ma (Su et al., 2019) is one of the major palaeoenvironmental events during the Cenozoic. The Red Clay Formation and loess deposits on the Chinese Loess Plateau, which are products of the Asian aridification, have been used to broadly constrain the drying history of the Asian interior during the Neogene (Porter, 2007). Studies on these aeolian sequences indicate that aeolian deposits start to accumulate on the Chinese Loess Plateau since ~7-8 Ma (Song et al., 2007), suggesting an initiation of Asian aridification during the late Miocene. Cenozoic uplift of the Tibetan Plateau had a profound effect upon the desertification in the Asian interior enhancing it (Guo et al., 2002). The timing of the uplift of the northern Tibetan Plateau has been under debate for decades and is still so until today, i.e. the onset of intensive exhumation in the southern Qilian Shan is thought to occur at ~18-11 Ma and at approximately 7 ± 2 Ma (Pang et al., 2019). A stepwise uplift during the middle Pleistocene is assumed as discussed in Wang et al. (2017). The uplift history includes the Qilian Shan (mountains) at the north-eastern border of the Tibetan Plateau, the area where the Heihe (engl. = Hei River) evolves from its upper reaches on the northern flanks.

Sediments from the Heihe and the more southeasterly flowing Shiyang Rivers are considered a major source for the Badain Jaran Desert and Tengger Deserts (Yang et al., 2012; Li et al., 2014; Wang et al., 2015; Hu and Yang, 2016). It has been argued that they belong to the dust sources for the Chinese Loess Plateau (Derbyshire et al., 1998; Sun, 2002; Che and Li, 2013; Pan et al., 2016; Yu et al., 2016). Today, the Heihe flows from the Hexi Corridor through the Heli Shan northwards into the Ejina Basin (synonymous: Gaxun Nur Basin), where it forms a giant alluvial fan (Fig. 1). When arriving at the lower reaches of the Heihe, the river carries not only the sediments eroded from the Qilian Shan, but also sediments washed from the western Beishan by ephemeral streams, and silty sands blown in from Mongolia in the North (Li et al., 2011; Che and Li, 2013). In addition, ephemeral channels originating from the eastern Altay Mountains indicate that large amounts of sediments are transported from the Mongolian Altay to the Ejina Basin. During the local wet periods of marine isotope stages (MIS) 3 and 5, and the mid-Holocene (Yang et al., 2010; 2011), strong fluvial input from the Altay Mountain ranges can be expected (Wünnemann et al., 2007).

The Ejina Basin has a lateral and vertical set of different sediment archives; i.e. lacustrine, playa-lacustrine, aeolian, and fluvial-alluvial (Wünnemann and Hartmann, 2002; Zhu et al., 2015; Yu et al., 2016). Coring the alluvial fan and underlying deposits at a central position within the basin is thus expected to yield a record that constrains the timing and mirrors the complex interactions between (i) Quaternary climate forcing of the Heihe discharge, (ii) a tectonic triggering of sediment pulses from the uplifting Qilian Shan, and (iii) internal sedimentation dynamics as they are characteristic of downstream alluvial fan progradation.

https://doi.org/10.5194/se-2019-163
Preprint. Discussion started: 4 November 2019

Solid Earth Discussions

The purpose of this study is to reconstruct the palaeoenvironmental change driven by climate and tectonical history in the area based on a sediment core from a distal position of the Heihe alluvial fan. The sediment is used for generating sedimentological data (i.e., grain size, XRF, XRD) that are augmented by information from selected bioindicators (ostracod and gastropod counts, n-alkane properties). Based on this multi-proxy dataset, the transition from more humid to more arid conditions in the Ejina Basin during the past 2.5 Ma years is reconstructed.
The studied core GN200 was drilled 2012 to a depth of 223.7 m, with Quaternary deposits reaching a thickness of 222.6 m. The Quaternary strata are underlain by sediments belonging to the regionally widespread 'Red Clay Formation', a set of alternating reddish aeolian sediments and carbonate-rich dark-reddish paleosols of Neogene (Porter, 2007) or late Cretaceous (Wang et al., 2015) age. The discussion on formation and composition of core GN200 considers the Ejina Basin fill as a prominent source of the Chinese Loess Plateau, because of its position in the upwind area.

2 Geographical, tectonic and climatic setting

The Ejina Basin is located in the Gobi Desert and part of the Alashan Plateau. It is an intramontane basin bordered by the Heli Shan in the south, the Beishan to the west, the Badain Jaran Desert to the east, and the Eastern Altay Mountains to the north (Fig. 1). The Ejina Basin has developed as a pull-apart-basin between the Northern Tibetan Uplands (i.e., the Qilian Shan) in the south and the Gobi Altay-Tien Shan mountain chain in the north (Becken et al., 2007). There is predominantly a left-lateral transpression acting on the regional upper crust due to the ongoing India-Eurasia collision (Cunningham et al., 1996). Neotectonic activity at the eastern edge of the Ejina Basin was interpreted based on graben geometry detected within crystalline basement using resistivity measurements (Becken et al., 2007; Hölz et al., 2007). Temporal and spatial patterns of fluvial-alluvial and lacustrine deposition are likely influenced by neotectonic movements; e.g., the western basin margin has a subsidence rate of ca. 0.8-1.1 m/ka (Hartmann et al., 2011), whereas in the north-eastern part of the basin the occurrence of seismites illustrates that seismicity has caused sediment rupture in close vicinity to normal fault lines (Rudersdorf et al., 2017). From south to north, the elevation ranges between 1300 m and 880 m above sea level (asl). The Heihe main stream entering the Ejina Basin has a length of more than 900 km (Li, X. et al., 2018) and originates from the slopes of the Qilian Shan in the south. From its upper reaches, it flows through the foreland of the Hexi Corridor and arrives at the lower reaches with two branches that are likely controlled by fault lines. Here, the Heihe builds up one of the world's largest continental alluvial fan systems in the endorheic Ejina Basin (Hartmann et al., 2011).
The Heihe basin covers an area of approximately 28,000 km2, while the total catchment of the Heihe system, connected with glaciers in the Qilian Shan (>4000 m a.s.l.), comprises roughly 130,000 km2. Along the distal part of the basin, three terminal lakes, namely Ejina, Sogo Nur and Juyanze, form a chain of lakes, which presently are all dried up (Wünnemann et al., 2007). Radiocarbon dating of ancient shorelines suggests that relative lake-level highstands occurred during MIS 3 (Wünnemann and Hartmann, 2002; Wünnemann et al., 2007b; Hartmann et al., 2011), although the 14C-based chronology for the area may

https://doi.org/10.5194/se-2019-163
Preprint. Discussion started: 4 November 2019

Solid Earth Discussions

underestimate the timing when compared with IRSL OSL results (Zhang et al., 2006; Wang et al., 2011; Long and Shen, 2015; Li et al., 2018; 2018b).

Presently the winter Siberian Anticyclone dominates the climate conditions in the basin (Chen et al., 2008; Mölg et al., 2013). The study area is characterized by a continental climate that is extremely hot in the summer and cold in the winter; the maximum daily temperature is 41 °C (in July) and the minimum daily temperature is -36 °C (in January). According to data from the Ejina weather station between 1959 and 2015 the mean annual temperature, precipitation, relative humidity, and wind speed were 9.0 °C, 36.6 mm, 33.7 % and 3.3 m/s, respectively, and the mean annual potential evaporation is as high as 3,755 mm (Liu et al., 2016). The growing season in the Ejina Basin is from April to September, during which time it is ice free and has seasonal Heihe river runoff. In contrast, the annual precipitation in the upper reaches in the Qilian Shan reaches 300-500 mm (Wang and Cheng, 1999; Wünnemann et al., 2007). Today, only the Ejina Oasis near Juyanze palaeolake receives ephemeral water input. Typical geomorphological features in the Ejina Basin are gravel plains, yardangs, playas, sand fields, and sporadically distributed mobile linear and barchan dunes (Zhu et al., 2015; Yu et al., 2016).

3 Methods

A rotational drilling system has been used for coring with 3 m long metal tubes 80-120 mm in diameter. The drilling took place in the centre of the Ejina Basin (42°3’12.96’’N, 100°54’14.4’’E) at 936 m asl. in a maximum distance to known fault lines. Once a core segment was retrieved, it was pressed out immediately, halved, described and photographically documented. Subtracting core gaps and overlaps the length of the core is 223.7 m with a recovery rate of 96%. On average sampling of 2 to 5 cm thick slices was done three times per meter or in accordance to sediment change for studying various sediment properties as described below (SI, supplementary information).

3.1 Non-destructive analyses

After core splitting several non-destructive analyses were carried out including visual description, optical line scanning, magnetic susceptibility analyses and XRF element scanning. Magnetic susceptibility measurements at 1 cm resolution were carried out on one core half using a Bartington MS2E sensor, while the other half was scanned with an Avaatech core scanner to determine semi quantitatively element compositions at 1 cm resolution. We applied a Rhodium tube at 150 µA and 175 µA with detector count times of 10s and 15s for elemental analysis at 10 kV (no filter) and 30 kV (Pd-thick filter). Element intensities were obtained by post-processing of the XRF spectra using the Canberra WinAxil software with standard software settings and spectrum-fitmodels. The element intensities depend on the element concentration but also on matrix effects, physical properties, the sample geometry, and hardware settings of the scanner (Tjallingii et al., 2007). We accepted modelled chi square values (χ^2) <2 as a parameter of measured peak intensity curve fitting for the relevant elements.

https://doi.org/10.5194/se-2019-163
Preprint. Discussion started: 4 November 2019

3.2 Grain-size distribution and endmember modelling analysis

Sediment grain-size distributions were determined using a laser diffraction grain size analyser (Malvern Mastersizer 3000). Prior to laser sizing the samples have been removed from organic carbon using H2O2 oxidation on a platform shaker until reaction ceased. The endmember modelling algorithm (EMMA) after Dietze et al. (2012) and modified by Dietze and Dietze (2019) was applied to the grain size data in order to extract meaningful endmember (EM) grain size distributions and to estimate their proportional contribution to the sediments. Results were translated into a core log that illustrates the succession and thickness of EM types. EM modelling analyses are used to address the main sediment types with their associated energy regimes.

3.3 Bulk mineralogy

The mineralogical composition of freeze-dried and milled samples was analysed by standard X-ray diffractometry (XRD) using an Empyrean PANalytical goniometer applying CuKα radiation (40 kV, 40 mA) as outlined in Petschick et al. (1996). Samples were scanned from 5° to 65° 2θ in steps of 0.02° 2θ, with a counting time of 4 s per step. The intensity of diffracted radiation was calculated as counts of peak areas using XRD processing software (MacDiff, R. Petschick in 1999). Mineral inspection focused on quartz, plagioclase and K-feldspar, hornblende, mica, calcite, and dolomite. Accuracy of this semi-quantitative XRD method is estimated to be between 5-10% (Gingele et al., 2001).

3.4 Clay mineralogy

The clay fraction (<2 µm) was separated using settling times according to the Atterberg procedure. Clay particles were oriented using negative pressure below membrane filters and they were mounted as an oriented aggregate mount on aluminium stubs with the aid of double-sized adhesive tape. The analyses were run from 2.49° to 32.49° 2θ on a PANalytical diffractometer. Two X-ray diffractograms were performed; one from the air-dried sample, one from the sample after ethylene glycol vapor saturation was completed for 12 hr. Estimation of clay mineral abundances focused on smectite, mixed-layer smectite/chlorite (10.6 Å), chlorite, and kaolinite (calculated to a sum of 100%) and is based on peak intensities. Clay analyses were made only from silt-dominated samples.

3.5 Fossil counts

Counts of fossils, i.e. ostracods and gastropods, have been conducted from 62 samples each comprising 40-85 g of dry weight. The size fractions of >250 µm, 250-125 µm, and 125-63 µm were examined after wet sieving using deionized water. Encountered shells were determined to at least the genus level. Shell fragments were also registered, but it has been excluded from further discussion due to the assumption that the material points to reworking. To yield meaningful numbers count results have been normalized to 100 g of dry weight.

https://doi.org/10.5194/se-2019-163
Preprint. Discussion started: 4 November 2019

3.6 Lipid biomarker analysis

Twenty-six samples were used for lipid biomarker extraction. The analysis focused on determining the concentration and downcore distribution of n-alkanes in the samples. In a second step, the δD signatures of two n-alkanes (nC29 and nC31) were measured. The work flow followed the sample processing as outlined in Berke (2018).

3.7 Statistical treatment

The mineralogical, geochemical, and lipid biomarker data are of compositional nature, which means that they are vectors of non-negative values subjected to a constant-sum constraint (usually 100%). This implies that relevant information is contained in the relative magnitudes and mineralogical and geochemical data analyses can focus on the ratios between components (Aitchison, 1990). In addition, log transformation will reduce the very high values and spread out the small data values and is thus well suited for right-skewed distributions (van den Boogaart and Tolosana-Delgado, 2013). Compared to the raw data, the log-ratio scatter plots exhibit better sediment discrimination.

Log-ratios can also minimize the problematic issue that element-compositional data from XRF measurements have a poorly constrained geometry (e.g., variable water content, grain size distribution, or density) and nonlinear matrix effects (Tjallingii et al., 2007; Weltje and Tjallingii, 2008). In addition, they provide a convenient way to compare different XRF records even when measured on different instruments in terms of relative chemical variations. Log-ratios of element intensities are consistent with the statistical theory of compositional data analysis, which allows robust statistical analyses in terms of sediment composition (Weltje et al., 2015).

Prior to PCA (principal component analysis) and k-means cluster analyses, a centred-log ratio (clr) transformation was applied to the data set following Aitchison (1990). This means element ratios were calculated from raw cps values and smoothed with a 5 pt running mean. Thus, cps values were clr transformed (Weltje and Tjallingii, 2008), whereby elements measured with 10 kV (Al, K, Ca, Ti, Mn, Fe) were calculated separately from 30 kV elements (Rb, Sr, S, Zr, Cr, Zn, Br).

3.8 Chronostratigraphy

The chronology of core GN200 is derived from magnetostratigraphy. Consolidated sediment samples were cut out manually as specimens and placed in plastic boxes of 1.8 cm*1.8 cm*1.6 cm. A total of 567 samples were used. Measurements of the natural remanent magnetization (NRM) and stepwise alternating field (AF) demagnetization were performed at the palaeomagnetic laboratory of Tübingen University using a 2G enterprises DC-4 K 755 squid magnetometer system with an in-line 3-axial AF demagnetizer. For data visualization and interpretation, the software package "Remasoft" (Chadima and Hrouda, 2006) was used, applying PCA (Kirschvink, 1980) for determination of palaeomagnetic directions. Because no control of drilling azimuths was available, the analysis and interpretation of palaeomagnetic directions is based solely on inclinations. All specimens were subjected to stepwise AF demagnetization (steps: NRM, 4, 6, 8, 10, 15, 20, 25, 30, 40, 50, 60, 80, and 100 mT). NRM intensities ranged from 0.01 to 4.2 mA/m with a median of 1.6 mA/m. Demagnetization runs usually provided interpretable results before reaching the noise level of the magnetometer. Most samples exhibited one-component-like or two-

https://doi.org/10.5194/se-2019-163
Preprint. Discussion started: 4 November 2019

component-like demagnetization behaviour. AF demagnetization characteristics and thermomagnetic runs proved magnetite as the main magnetic carrier of the characteristic remanent magnetization (ChRM). The resulting polarity sequence is based on 281 ChRM directions, determined by PCA with a minimum of 4 consecutive demagnetization steps and mean angular deviation (MAD) <10° (Fig. 7). A minimum of two subsequent ChRM directions with inclinations >/< +/- 20°, were required for defining a polarity interval. Where necessary, also PCA components with MAD >10° or with demagnetization paths including to the origin (for the final component) were used to support the interpretation. Overprints of recent Earth Magnetic Field (EMF; parallel to normal palaeofield direction), which cannot be separated from the palaeoremanence, lead to better grouping of apparently normal palaeodirections and a more scattered distribution of reverse palaeodirections.

We augment the relative ages of the palaeomagnetic datasets with absolute ages using simple burial dating based on in situ-produced cosmogenic nuclides (e.g., Balco and Rovey II, 2008; Granger, 2014). Five samples from different depths were sieved, different grain sizes cleaned, and prepared according to protocols outlined in Schaller et al. (2016). Chemical preparation of the samples was conducted at the University of Tübingen, Germany. 10Be/9Be and 26Al/27Al ratios were measured at the AMS facility at Cologne, Germany. The age calculation for simple burial dating is based on a MatLab script of Schaller et al. (2016). The decay constants used for 10Be and 26Al are (4.997 ± 0.043) x10-7 (Chmeleff et al., 2010; Korschinek et al., 2010) and (9.830 ± 0.250) x10-7, respectively (see Norris et al., 1983). We used sea level-high latitude (SLHL) production rates of 3.92, 0.012, and 0.039 atoms/(g(qtz) yr) for nucleonic, stopped muonic, and fast muonic 10Be production, respectively (Borchers et al., 2016; Braucher et al., 2011). The SLHL production rates for 26Al are 28.54, 0.84, and 0.081 atoms/(g(qtz) yr) for nucleonic, stopped muonic, and fast muonic production, respectively (Borchers et al., 2016; Braucher et al., 2011). These production rates result in a SLHL 26Al/10Be ratio of ~7.4. We then scaled the SLHL production rates to the sample locations of this study based on the online tool of Marrero et al. (2016) using the scaling procedure "SA" from Lifton et al. (2014). Depth scaling of the production rates is based on nucleonic, stopped muonic, and fast muonic adsorption lengths, which are 157, 1500, and 4320 g/cm2, respectively (Braucher et al., 2011). The density of 2.4 ±0.2 g/cm3 is assumed to be constant over the depth of the core.

Depth-to-age transformation was carried out by linear interpolation between the ground surface (present) and a double-dated core portion between 60 m and 53 m core depth from both techniques, i.e., palaeomagnetic and radionuclide results. Based on lithostratigraphy the portion between 223.7 and 222.6 m core depth is interpreted to belong to the pre-Quaternary (>2.6 Ma) Red Clay Formation, a widely studied set of strata that is mainly of aeolian origin and widely spread across NW China (Kukla, 1987; Porter, 2007; Sun et al., 2010; Shang et al., 2018).

4 Results

4.1 Sediment stratigraphy

Three main sedimentary units are identified in core GN200 (Fig. 2, supplementary information SI). From bottom to top they are as follows: Unit A (223.7-217.0 m) is dominated by coarse-grained layers (fine- to medium-grained sand) interbedded with

https://doi.org/10.5194/se-2019-163
Preprint. Discussion started: 4 November 2019

fine-grained sediments (clayey silt). Colours change on a submeter-scale from red and orange in the sandier parts to grey in the silt-rich layers. Sediment change can be both sharp and transitional. Occasionally cm-thick white layers indicate carbonate enrichment in the sandy layers. Unit A includes deposits that are interpreted to belong to the Red Clay Formation; between 223.7 and 222.6 m a fanglomerate at the core bottom is overlain by red medium sand. This subunit has a sharp boundary with the grey (anoxic) medium sand layers covering them.

Unit B (217.0-110.0 m) has a succession of banked clayey silt with an increasing frequency of intercalated coarser grained layers dominated by very fine sand to fine sand towards the top of the unit. Silt portions can stretch over several meters upcore and turn from grey (217.0-200.0 m) to brown-olive colours (200.0-177.0 m). Remarkably, sequences of clayey silt between 210.0 and 200.0 m show successions of mm-thick laminations of white and grey to orange laminae. Brown to orange colours appear in the middle to upper part of the unit (177.0-110.0 m). Some layers containing coarse sand to very fine gravel form a top subunit (between 120.0-110.0 m). Counts of macrofossils are overall low, if samples are not barren at all. Ostracod remains can be found occasionally in layers scattering above 196 m core depth and up to the top of the unit. They are admixed to greatest extent (to double-digit numbers) in coarse silty sediments; especially at core depths 181.5 m, 138.0-137.0 m, 128.0-127.0 m, 121.0 m, and at 114.8 m. Gastropod shells are found even more rarely. They are encountered in fine silt at 177.6 m and 138.7 m core depth and in coarse silt layers at 120.6 m and 113.7 m (fine silt). Remarkably, no fossils occur in the laminated fine silt layers between 210.0 and 200.0 m and between 173.0 and 172.0 m.

Unit C (110.0-0.0 m) is a succession of fine and medium sand layers interbedded with silt banks that decrease in frequency towards the top. The gradational increase in fine silt content in these silt banks is paralleled by a loss of the clay fraction. Depending on dominating grain sizes colours change from yellow, grey and orange in the sandier layers to light-red in the silt banks. At core depths between 28.5 and 27.5 m and between 10.0 and 7.0 m black soft mud occurs, which likely represents lake sedimentation. At 103.2 m, at 99.3 m, at 68.6 m, and at 43.2 m core depth noteworthy accumulations of ostracod shells were found. Dominating grain size fractions in layers containing ostracods range from coarse silt to fine and medium sand. Gastropod shells were found only in few layers at 103.2 m, 102.9 m, and 99.9 m depth. The dominating grain-size fractions in these sediments range from coarse silt to fine and medium sand.

A graphic log of the sediment column derived from visual logging and EMMA-derived endmember calculations is presented in Fig. 2. For completion the sample population and EM modelling results are added. Most of the GN200 samples have a polymodal grain size distribution. The EMMA algorithm produces a five-EM model that envelops all main modes. This explains more than 99.6% of the total variance (see App.). EM 5 is associated with medium to fine sand and a primary mode at ~400 µm and a subordinate mode at 37 µm (8.6%); EM 4 represents fine sand with the main mode at 180 µm (34%); EM 3 is composed of silty sand with the main mode at 92 µm (11%); EM 2 is composed of medium silt with a primary mode at 18 µm and a subordinate mode at 360 µm (27%). Remarkably, EM 2 is similar as EM 5 but with reverse order of mode precedence. EM 1 is composed of clayey silt with a main mode at 4 µm and a subordinate fine sand fraction admixed (19%). Surficial processes and landforms producing sediments as found in GN200 are typically fluvial, fluvial-aeolian, levee and overbank deposition, sheetflood and surface wash (playa) and lacustrine processes (e.g. Zhu et al., 2015). Fig. 2 illustrates the frequency

https://doi.org/10.5194/se-2019-163
Preprint. Discussion started: 4 November 2019

and depositional interpretation of sediment types in core GN200. Apart from unit A the frequency of coarse-grained (sand-dominated) layers generally increases from the bottom of unit B to the top of unit A. The appearance of the first prominent sand layer that is several meters thick in size is used to set the boundary between the two units B and A.

4.2 Dating from palaeomagnetism and radionuclide concentrations

The polarity sequence from core GN200 starts at the top with normal polarity and has several longer intervals of reverse polarity further downcore between c. 60-80 m, 100-135 m, and 170-225 m (Fig. 3). Given that during the Brunhes chron only few very short events of reverse polarity have occurred (Singer, 2014; Cohen and Gibbard, 2019), which cannot explain any longer intervals of reverse polarity, the polarity boundary at c. 60 m can be correlated to the Brunhes/Matuyama (B/M) boundary (0.773 Ma). Locating the exact position of the B/M boundary in the record, however, may be a matter of discussion. The EMF behaviour at the B/M boundary is obviously rather complex (Singer, 2014) and the limitations of the sampling (no azimuths) and demagnetization procedures (no thermal demagnetization possible) do not allow to disentangle the effects of palaeofield behaviour, lock-in-mechanism, and to separate different palaeofield and recent field components completely. In most of the downcore normal polarity intervals, AF demagnetization behaviour of specimens looks one-component-like, whereas in reverse intervals and near reversals it frequently appears more complex and may exhibit two components of magnetization, which cannot be separated sufficiently. From about 55 to 60 m, shallow normal and reverse components with inclinations < 20° can be observed in many samples. Slightly changing the criteria for defining polarity intervals could shift the polarity boundary (B/M boundary) close to 55 m. Based on the polarity pattern and assuming sediment accumulation rates of similar magnitude, the well-defined intervals of normal polarity at about 85-95 m and 150-170 m may be tentatively correlated to the Jaramillo (0.988-1.072 Ma) and Olduvai (1.788-1.945 Ma) subchrons. However, it is unclear whether two very short intervals of normal polarity at around 115 m and 125 m represent palaeofield behaviour or are artefacts caused by recent field overprints. The lowermost part of the drill core between 172.0 and 222.6 m shows reverse polarity, which is separated by a hiatus from the rest of the polarity sequence.
Burial dating based on in situ-produced cosmogenic nuclides provides three out of six measurements of 10Be and 26Al concentrations, which have produced reliable results; namely GN200 19a, GN200 21a, GN200 34b (Tables 1 and 2). In contrast, the remaining three samples produced signals close to blank and are discarded from interpretation (GN200 68 a, GN200 102a, GN200 102a, Tables 1 and 2). The samples from core depths 19.1 m, 20.3 m, and 53.1 m had quartz portions high enough for robust measurements (Tables 1 and 2). The upper two samples have yielded ages >2 Ma BP, the one at 53.1 m core depth has an age of 0.84 ±0.12 Ma BP. When accepting the lower sample age, the two upper ages are reversals, which can be explained by reworking of old material that has been eroded and transported from the catchment prior to its final deposition in the Ejina Basin (Fig. 4). Given the error bar of the 53.1 m sample (0.84 ±0.12 Ma) the radionuclide age overlaps with the Brunhes-Matuyama boundary (0.773 Ma BP) on the geomagnetic time scale and which itself has an error bar of ±1% at this chron boundary (Singer, 2014). If this geochronological interpretation is true, it would back up the prominent 20 m thick event with negative inclination below 60 m core depth as belonging to the Matuyama chron.

https://doi.org/10.5194/se-2019-163
Preprint. Discussion started: 4 November 2019

From magnetostratigraphy the first-order depth-to-age relationship produces a mean sedimentation rate of 9 cm/ka during the last 2.58 Ma in the Ejina Basin (Fig. 4). This assumes an overall balanced change of accumulation and erosion across glacial-interglacial cycles in the area. If the radionuclide dating at 53.1 m (0.84 ±0.12 Ma BP) is included, this sedimentation rate slightly decreases to 6 cm/ka in the upper 53 m, whereas the lower 169 m core have a slightly increased sedimentation rate of 10 cm/ka.

4.3 Bulk sediment properties

The graphic log of the GN200 sediment column is combined with downcore XRF element distribution in Figure 5. From the bottom to the top elemental relative concentrations show that sandy sediments of unit A are Al-K dominated, whereas fine silty lacustrine deposits at the bottom of unit B are more Mn- and K-Al dominated. Playa deposits in the lower part of unit B can be characterized by Ca-Ti or by Al-K dominated sediments. The upper part of unit B holds an alternation of Mn and Al-K dominated sediments. In unit C sediments change from the Al-K type to greater portions of Ca-Ti dominated sediments. PCA calculations from 10 kV XRF data (i.e., the main siliciclastic components K, Ca, Ti, Mn, and Fe) reveal that Ca and Ti define the first principal component explaining 40.2% of the total variance. The second component is described by Al and Mn explaining 29.3%. Ca likely reflects a combination of carbonate (detrital or authigenic) content and feldspar composition. In this way it can highlight both fine-grained and coarse-grained sediments. The Ca/Ti ratio illustrates that Ti is enriched especially in unit A as also is the case with K. Mn is depleted when compared with the overlying sediments of unit B and unit A. Within unit B Ca most prominently dominates sediment layers between 182 m to 165 m. Further upcore there are individual layers in unit C at 105-102 m, 91 m, and 68 m, where Ca distinctly dominates over Ti.

Remarkably, the variability of K is increased when more sandy sediments are intercalating with playa deposits; this is valid between 175 and 165 m and for most of unit C. Mn excursions are paralleled by enrichment in S and distinct peaks in magnetic susceptibility. This is particularly true for the lacustrine sediments at the bottom of unit B and playa sediments in the middle part of unit B between 168 and 159 m. S is also enriched between 105 and 102 m, in this case without a marked occurrence of Mn and magnetic susceptibility, but paralleled by peaks of Ca.

As for unit B counts of macrofossils are overall low in unit C, if samples are not barren at all. Ostracods are especially found in double-digit numbers at core depths 103.8 m, 68.6 m, 43.4-43.3 m, 38.7 m, 38.1 m 37.6 m 34.9 m, 33.9 m, and 31.9 m. Ostracod communities are dominated by Ilyocypris sp., which prefers fresh- to brackish-water habitats (Mischke, 2001; Yan, 2017). A high abundance of ostracod valves can be an evidence for short transport with a proximate burial (Mischke, 2001). Gastropods are found in considerable double-digit numbers only in sandy to silty sediments between 103.9 m and 99.9 m depth (Fig. 5). They are represented by Radix peregra, which thrives in waters with a salt content of up to 33.5 ‰ (Verbrugge et al., 2012).

Bulk mineralogical composition is characterized by high counts of quartz and feldspar in unit A (Fig. 6). Feldspar is relatively enriched over quartz when compared with units B and C. Dolomite is decreased with respect to calcite in unit A when compared to units B and C. Mineralogical differences between units B and C are less distinct, but best expressed with lower quartz and feldspar amounts in B than in C, where the frequency of sandy layers increases. Hornblende and dolomite do not have distinct trends, but show individual peaks scattered units B and C. They appear to be connected to individual sediment layers; i.e. hornblende at 171.0 m, dolomite at 77.0 m. Calcite is found nearly continuously in unit B with respect to the average of all inspected minerals. Towards the upper 40 m of unit C, which are dominated by a succession of sand layers, the calcite amount decreases.

Smectite in the clay mineral record clearly increases in playa lake sediments of unit B (Fig. 7). In contrast, mixed-layer minerals (i.e. chlorite/smectite) have peak occurrence only in unit C, where kaolinite is low. In unit B and C kaolinite is non-conclusive as is chlorite at a first glance. However, there is an upcore trend towards higher chlorite amounts; between 223.7 and 130.0 m the average is 20%, whereas above 130.0 m core depth it increases to 27%.

4.4 Lipid biomarker and δD record

Evidence for hydrologically driven vegetation change in the Ejina Basin is provided from biomarker data (Fig. 8). The concentration and distribution of n-alkanes allow insight into the vegetation dynamics in the Ejina Basin and its catchment. As outlined in Koutsodendris et al. (2018) vegetation contains straight-chain hydrocarbons and the length of the n-alkanes can be linked to original plant types. For example, nC17-nC19 are derived from phytoplankton, nC23-nC25 originates from submerged aquatic macrophytes, nC27-nC35 belong to epicuticular waxes of higher terrestrial plants (Eglinton and Eglinton, 2008; Aichner et al., 2010). The short-chain nC19 n-alkane is most abundant between core depths 64 m to 44.1 m. Concentrations though are low and range between 0.048 and 0.068 µg/g dry weight of sediment. Mid-chain n-alkanes such as nC23-nC25 can be found in samples between 217 m to 44.1 m and have higher concentrations with a maximum value of 0.123 µg/g dry weight occurring at 159.2 m depth. Long-chain n-alkanes nC27-nC35 are dominant in core GN200 with a maximum value of 0.928 µg/g dry weight at 215.45 m core depth. Selected concentrations and stratigraphic distributions of n-alkane data are shown as centre-log ratios in Fig. 8. In addition, P(aq) is added, which is a proxy ratio that highlights the terrestrial versus the emergent aquatic versus the submerged aquatic macrophyte origin of the lipids (Ficken et al., 2000). It becomes clear that with few exceptions much of the n-alkanes have low P(aq) values around 0.1 and likely originate from terrestrial rather than aquatic sources (Fig. 8).

δD wax values derived from terrestrial plant n-alkanes record the isotopic composition of the plant water and, by extension, temperature and precipitation (Sachse et al., 2012). As discussed in Koutsodendris et al. (2018) δD wax potentially serves as a sensitive recorder of palaeoclimatic variability. In the GN200 samples, δD measurements based on leaf-wax nC29 and nC31 alkanes yielded δD values between -189‰ and -148‰, and -184‰ and -148‰, respectively. The δD wax values from the nC29 and the nC31 alkanes are highly correlated ($r2 = 0.95$), which confirms their common origin from terrestrial plants.

https://doi.org/10.5194/se-2019-163
Preprint. Discussion started: 4 November 2019

5 Discussion

Earth surface dynamics include a variety of processes that result in mixing of grain size subpopulations in sedimentary systems. Sediment from different sources can be transported and deposited by a multitude of sedimentological processes that have been linked to climate, vegetation, geological and geomorphological dynamics as discussed in Dietze and Dietze (2019). The record from core GN200 has variable grain size distributions (Fig. 2C) indicating various transport processes that have shaped the depositional environment in the endorheic Ejina Basin. The interpreted endmembers fluvial, aeolian, playa (or sheetflood), and lacustrine processes have smooth transitions reflecting several energy regimes as is typical for desert and alluvial fan environments (Blair and McPherson, 1994). Only recently Yu et al. (2016) described alluvial gravels, fluvial sands, aeolian sand, sandy loess, and lacustrine clays as main sediment types that can be found in the Ejina Basin. Interpretations of nearby cored sediments (230 m long core D100) have related the coarse-grained portions -resembling EM 5 in GN200 - to high-energy fluvial transport from local areas such as the northern (Gobi-Altay-Tienshan range) and western (Beishan) catchment of the basin (Wünnemann et al., 2007b). Following this study well-sorted fine sand as found in core D100 resembles EM 4 in GN200 and is likewise interpreted as being of aeolian to fluvial origin. Coarse and fine silt deposits resemble EM 3 and EM 2 and indicate playa-like depositional environments under different energy systems. Successions of finer to coarser silt layers building up much of unit B suggest that the depositional processes involved alternating hydrological conditions. Possibly this includes occasional desiccation events in the playa plain as is visible from individual layers of well-sorted fine sand, which suggest aeolian deposition at the site. On the other hand, bioindicators such as ostracods and gastropods document temporarily subaquatic conditions as are found in ponds and playa-lakes. This is also true for unit B sediments, which are interpreted to represent playa-lake environmental conditions.

Formation and transformation of clay minerals in soil profiles and regoliths is determined by an interaction between the geology, drainage control by geomorphology, and the climate of the source terrain (Singer, 1984; Hillier, 1995; Wilson, 1999; Dill, 2017). Tracking clay mineralogical changes in the detrital sedimentary compositions of the Ejina Basin by means of XRD data thus can aid the interpretation of environmental changes. Variations in the Ejina Basin clay mineralogy appear to be closely linked to main changes in depositional environments: mixed-layer clays characterize sediment layers belonging to the Red Clay Formation (223.7-222.6 m) and overlying deposits that have incorporated reworked portions of it (222.6-217.0 m) (unit A), smectite-rich clay characterizes the playa environment (large parts of unit B), and chlorite-rich clays are transported with Heihe river sediments (unit C with overlap to unit B).

Complementary detrital and authigenic signals of sediment origin are preserved in the bulk XRD and XRF data and can support the interpretation of sediment environments (e.g. Hillier, 2003; Jeong, 2008; Song et al. 2009). As with the clay signals the unit A sediments, which belong to the Red Clay Formation, are well defined by XRD bulk data; i.e., unit A is markedly dominated by quartz and feldspar when compared with unit B and unit C (Fig. 6).

SEM and XRD analyses of samples with higher concentrations of sulphur from nearby core D100 yielded evidence of gypsum formation when sulphur increased (Wünnemann et al., 2007). It has been interpreted as pointing to a stepwise shrinkage of the water body under dry-warm conditions. Within the playa-lake succession in unit B prominent peaks of magnetic susceptibly along with sulphur likely indicate greigite (Fe3S4) formation (Fig. 5). Preservation of greigite can occur in terrigenous-rich and organic-poor sediments and is proposed to result from a dominance of reactive iron over organic matter and/or hydrogen sulphide, which otherwise would favour pyritization reactions (Blanchet et al., 2009). In fact, unit B sediments do not contain organic matter based on a set of TOC measurements using an elemental analyser, which produced results only below the detection limit of 0.1% scattered over the unit (not displayed).

Referring to results from Koutsodendris et al. (2018) the record of n-alkanes can show that glacial and interglacial periods are likely preserved in the record; GN200 δD values range greatly between -145‰ (interglacial) and -190‰ (glacial). Considering that the Ejina Basin is located in the mid-latitudes of the Northern Hemisphere and exhibits strong seasonal temperature variability, leaf wax δD values in GN200 are primarily a measure of temperature and indicative of the origin of moisture following interpretations given in Koutsodendris et al. (2018) and which are based on Gat (1996), Huang et al. (2004), Seki et al. (2011), and Sachse et al. (2012). As such, on glacial/interglacial timescales more negative δD wax values should reflect colder rather than wetter conditions and/or a more distant water source as interpreted in Koutsodendris et al. (2018). Koutsodendris et al. (2018) further propose that the δD value of nC29 and nC31 alkanes can be affected by evaporative deuterium enrichment of leaf water caused by enhanced evapotranspiration under low atmospheric humidity based on Sachse et al. (2006), Seki et al. (2011), and Rach et al. (2014). In this way GN200 samples from dry glacials can be also affected by evapotranspiration. As such, the actual difference between the interglacial and glacial end members in δD wax values was likely even larger than suggested by the available values from core GN200 following Koutsodendris et al. (2018). The discontinuous GN200 biomarker record reveals several intervals where glacial-to-interglacial changes are preserved: between 217 to 210 m a change from glacial to interglacial conditions and between 165 to 148 m a cycle from interglacial to glacial and back to interglacial conditions. Scattered samples further upcore suggest both glacial (128 m, 44 m) and interglacial (64 m, 46 m) conditions. However, the succession may be debatable, because of sediment reworking assumed for much of unit B and A sediments.

In contrast to a former chronology from drilling into the Ejina Basin (i.e., 230 m long core D100, Wünnemann et al., 2007), where a palaeomagnetic dataset has been interpreted to encompass 250 ka BP, the playa-lake environment is now interpreted to extend further back in time. The onset of more humid conditions with lake sedimentation must date back to into the early Pleistocene (>2 Ma BP) based on the Brunhes/Matuyama chron boundary at 60 m core depth and the occurrence of the Jaramillo and Olduvai subchrons interpreted in this study (Figures 3 and 4). A further linear extrapolation of the time axis down to the core bottom is based on the following assumptions: (i) the Gauss chron (normal polarity) is not detected in the record, thus, GN200 reaches the onset of the Matuyama chron at maximum (2.59 Ma). Between 222.6 and 223.7 m a reversal to normal (Gauss?) is indicated, but statistically not significant. But the extrapolated value comes close to the assumed value from linear extrapolation. (ii) The depositional sequence does not change prominently; the core portion between 222.6-172.0 m has an alternation of fluvial-alluvial layers intercalating with playa-lacustrine sediments typical for desert environments. (iii) Unit A sediments (222.6-217.0 m) are interpreted to be reworked material from the underlying Red Clay Formation implying that the Neogene likely was at proximity. (iv) Possibly there is a hiatus between the lowermost layers (223.7-222.6

https://doi.org/10.5194/se-2019-163
Preprint. Discussion started: 4 November 2019

m) and the overlying sediments (<222.6 m); the core bottom (223.7-222.6 m) consists of fanglomerate sediments and red-coloured medium sandy sediments that are interpreted to represent the Red Clay Formation, whereas sediments above a sharp boundary at 222.6 m turn into grey-coloured fine sand to silt layers. The transition from an oxic to an anoxic environment is distinct.

The resulting linear first-order depth-to-age relationship suggests that on a Quaternary time scale the overall sedimentation rates in the Ejina Basin are fairly constant. This matches results from Willenbring and von Blanckenburg (2010), who show that during the Late Cenozoic global erosion rates and weathering are stable; thus demonstrating that erosion and accumulation rates are balanced on Ma-time scales. Even though at smaller scales one may distinguish between independent histories at the subcontinental and basin scales, our age model accepts that extrusion and crustal shortening are complementary processes that have been successively dominant throughout the India-Eurasia collision history (Métivier et al., 1999). This is thought to affect also the Ejina Basin sediment history, which receives detritus from the Qilian Shan in the northern Tibetan Upland. On long time scales (Ma) the sedimentation rates in the Ejina Basin are low, i.e., 9 cm/ka. For comparison, the Tarim and Qaidam basins in the Tibetan Upland received 1 m/ka during the last 2.0 Ma (Métivier et al., 1999).

Other results from surface dating using radionuclides show that the Gobi Desert in the northern margin of the basin developed 420 ka ago, whereas the surfaces that developed from alluvial plains in the Heihe drainage basin formed during the last 190 ka (Lü et al., 2010). The latter developed gradually northward and eastward to the terminal (palaeo) lakes of the river. These temporal and spatial variations in the Gobi Desert are likely a consequence of alluvial processes influenced by Tibetan Plateau uplift and tectonic activities within the Ejina Basin. This largely overlaps with results from Hetzel et al. (2002), who inferred Qillian Shan strike-slip movements from a series of incised terraces dating back to 40 to 170 ka BP using cosmogenic nuclide dating. In addition, Li et al. (1999) suggest that tectonic activity was more intense around 160 ka and 40 ka BP based on 14C and TL dates from dissected alluvial fans in the Hexi Corridor. The relationship between tectonics, surface processes and superimposed climate fluctuations are thus reasonable for at least the past 200 ka. Lü et al. (2010) put forward that possible episodes of Gobi Desert development within the last 420 ka indicate that the advance/retreat of Qilian Shan glaciers during glacial/interglacial cycles might have been the dominant factor to influencing the alluvial intensity and water volume in the basin. Intense floods and large water volumes would mainly occur during the short deglacial periods.

Thus, sedimentologic interpretations of core GN200 have regional palaeoclimatic and palaeotectonic implications. The presence of lacustrine and playa-lacustrine deposits in the Ejina Basin supports previous interpretations of semiarid or arid climatic conditions including indicators such as evaporitic (i.e. sulphur) and possibly greigite bearing deposits in the NW Gobi Desert during the Pleistocene. Although this climatic interpretation is not new, it is now refined to stretch back over a longer time window into the early-to-mid Pleistocene. Former studies presented sediment archives from desert and lake sediments in the area only until MIS 3 (e.g. Hartmann and Wünnemann, 2009; Hartmann et al., 2011) or MIS 5 (Li et al., 2018) or until 250 ka BP (core D100, Wünnemann et al., 2007).

The climatic interpretation is nevertheless general and the data are not sensitive enough to determine absolute amounts of precipitation (and thus distinguish between arid and semiarid) to decide whether precipitation was seasonal. Moreover, n-

https://doi.org/10.5194/se-2019-163
Preprint. Discussion started: 4 November 2019

alkane data suggest that temporal resolution is at best on a glacial-to-interglacial timescale. It does not account for unknown detailed change of erosion and accumulation in the Ejina Basin and in the Heihe alluvial fan environment.

What effect, if any, did tectonic pulses along the Hexi Corridor to Heli Shan boundary fault have on sedimentation trends in the Ejina Basin? Predictably, tectonic uplift in the source area, i.e. Qilian Shan (Zheng et al., 2017), should generate periods of regression and/or coarse clastic influx in the adjacent basin, i.e. the Hexi Corridor. It is beyond the scope of this paper to discuss this problem further, but perhaps the cores extracted from the Hexi Corridor (DWJ, XKJD) presented by Pan et al. (2016) act as a support of the possibility of tectonic control on sedimentation in the Ejina Basin. The authors concluded that the Heli Shan opening occurred around 1.1 Ma BP and allowed the Heihe to flow northward into the Ejina Basin. The geomorphological change in catchment size, presumably triggered by block movement and/or uplift, would then provide a tipping element that finally led to the expulsion of the distal lake environment in favour of an extensive alluvial fan environment. Alluvial fan progradation may be flanked by changing evaporation rates and humidity changes on glacial-to-interglacial timescale though.

In this sense the first order chronology of the GN200 is confirmed by findings of Pan et al. (2016) and their cores from the Heihe fluvial/alluvial plains in the Hexi Corridor. Thus, the mega-sequence forming unit C in GN200 is a coarsening up succession that represents the arrival and progradation of the Heihe alluvial fan in the Ejina Basin. An upcore enhanced chlorite load, which to some extent is paralleled by an enhanced dolomite load in units B and C, may support this interpretation; chlorite is known to be exposed in basaltic bedrock outcropping in the Qilian Shan and so is dolomite; both minerals are interpreted to be indicative provenance minerals of the southern catchment (Song et al., 2009; Schimpf, 2019), which increase in the Ejina Basin with the arrival of Heihe river sediments.

Pan et al. (2016) discussed a previous study, which suggested that the Shiyang River (400 km SE from Heihe) formed approximately 1.2 Ma (Pan et al., 2007), based on studies of the highest fluvial terraces. This age is consistent with the formation age of the Tengger Desert (Li et al., 2014). A recent study in the Badain Jaran Desert (Wang et al., 2015) suggested a formation age of at least ~1.1 Ma based on electron spin resonance (ESR) dating of aeolian sands from a 310 m drilling core. First-order dating of the Ejina Basin sediment fill as recovered in GN200 brings additional input into the debate on the timing of when this part of the Gobi Desert started to serve as a sediment source for downwind sediment accumulation such as in the Badain Jaran and Tengger Deserts and ultimately the Chinese Loess Plateau (Chen et al., 2006). The onset of the Ejina alluvial fan formation coincides with increased sedimentation rates on the Chinese loess plateau <1 Ma (Sun and An, 2005; Sun et al., 2010), suggesting that the Heihe sediment fan formation may have served as a prominent upwind sediment source to it. Figure 9 summarizes a depositional model of a progressively northward propagation of the Heihe alluvial fan environment into the Ejina Basin.

The arrival of Heihe sediments coincides with the climate transition during the Mid-Pleistocene. Koutsodendris et al. (2018) discuss that this time, the Mid-Pleistocene Transition (MPT; ~1250-750 ka), is characterized by a change in global climate dynamics associated with the expansion of polar ice sheets (see also Head and Gibbard, 2015; Clark et al., 2006; Raymo et al., 2006). Koutsodendris et al. (2018 and references used therein) discuss further that as a consequence of global cooling during the MPT glaciers formed in high-elevation settings in the low and middle latitudes of both hemispheres. Glacial-interglacial contrasts strengthened after 1200 ka according to Diekmann and Kuhn (2002) based on analysing bulk parameters of a marine sediment core from the southeastern South Atlantic.

Terrestrial records in Central Asia mirror MPT cooling (An et al., 2011; Prokopenko et al., 2006; Sun et al., 2010) and temperature and ice volume change during glacials and interglacials as reviewed in Koutsodendris et al. (2018). For example, core SG-1 from the Qaidam Basin has a record of pollen concentration, CaCO3 content, and magnetic susceptibility that closely tracks global ice volume (Lisiecki and Raymo, 2005) and monsoonal activity in Central Asia (An et al., 2011; Sun et al., 2010) on glacial/interglacial time scales according to Koutsodendris et al. (2018). It has been concluded from this sediment core that the Tibetan Plateau may have been glaciated at least to some extent during the MPT based on palynological and δD wax-based palaeohydrological data analysis (Koutsodendris et al., 2018). From the same Qaidam Basin record (SG-1) other sediment properties show clear glacial/interglacial humidity changes across the MPT based on magnetic and palynological proxy data (Herb et al., 2013; 2015). Even though GN200 covers the same age range the discontinuous proxy record in concert with the unknown succession of accumulation and erosion hampers a detailed analysis comparable to the palaeolake sediments from the Qaidam Basin. In addition, it is not yet clear, whether GN200 lipid biomarkers have been transported by wind from remote areas or by fluvial input from the catchment or as a mixture of both.

6 Conclusions

A 223 m long core (GN200) was drilled in the central part of the Ejina Basin. Multiple parameter analysis of sediment properties illustrates that the basin is filled primarily with playa-lacustrine deposits in the lower half and holds a transition to an increasing frequency of fluvial-alluvial layers in the upper half. The lake environment shrank north-eastwards when from the southwestern part fluvial-alluvial deposits accumulated in a large sediment fan. The Quaternary playa-lacustrine to fluvial-alluvial deposition is presumably separated by a hiatus from the Neogene/Upper Cretaceous aged Red Clay Formation, which is encountered in the bottom six core meters.

The tipping element that induced the transformation from an early-to-mid Pleistocene more humid and playa dominated environment to a more arid environment dominated by an alluvial fan deposition is likely triggered by uplift and tectonic activity in the upper reaches of the Heihe. This environmental framework is in accordance with the regional environmental background inferred from other studies. It suggests that the contribution of dust from the Ejina Basin to the Chinese Loess Plateau was relatively limited during the early Quaternary, but may have increased after the progradation of the sediment fan into the basin after about <1 Ma.

7 Figure captions

Figure 1. (A) The study site is located in an area dominated by left-lateral transpression due to the ongoing India-Eurasia collision. GTSFS=Gobi Tien Shan fault system, QSTF=Qilian Shan thrust front, ATF=Altyn Tagh fault. (B) The Heihe alluvial

https://doi.org/10.5194/se-2019-163
Preprint. Discussion started: 4 November 2019

fan formation (white dotted line) covers much of the Ejina Basin. Fault lines (confirmed / inferred) are intersecting the study area (Rudersdorf et al., 2017, modified). GN200 marks the coring site. (Image source: SRTM under CC BY-SA)

Figure 2. (A) GN200 graphic log with sediment units and litho codes deduced from grain size dominating endmembers (EM) (based on Dietze and Dietze, 2019). Interpretation of depositional environment is added. (B) Illustrated endmember calculation results and (C) sample population (see also Appendix). (D) SEM images and core scan examples for the main sediment types as defined by endmember interpretation.

Figure 3. Litho- and magnetotstratigraphy of core GN200. The geomagnetic polarity time scale (GPTS) is from Cohen and Gibbard (2019).

Figure 4. Age-depth-relation in core GN200. The first order age model is related to the interpreted magnetostratigraphy. Radionuclide datings are given in addition. For more discussion see the text.

Figure 5. GN200 core with selected XRF elemental distribution, magnetic susceptibility (SI), and presence of ostracods and gastropods. S clr has been calculated from 30 kV elements. Interpreted greigite occurrence is marked, in addition. (clr = centred-log ratio)

Figure 6. GN200 core with mineral distributions from XRD bulk measurement. Qz=quartz, Fsp=feldspar, Plag=plagioclase, Hb=hornblende, Do=dolomite, Cc=calcite. (clr = centred-log ratio)

Figure 7. GN200 core with clay mineral distribution and interpretative labels. Smec=smectite, ML=mixed layers minerals, Kao=kaolinite, Chl=chlorite. (clr = centred-log ratio)

Figure 8. GN200 core with lipid biomarker distribution. Colored areas highlight interpretation of lipid origin (based on Ficken et al., 2000) and palaeoclimate interpretations. (clr=centred-log ratio)

Figure 9. Conceptual model illustrating the progradation of the Heihe alluvial fan into the Ejina basin.

8 Table list

Table 1: Information for burial ages from drill core GN200

Table 2: Analytical information for burial age calculations

9 Appendix

Appendix 1. Default graphical output of robust.EM() as part of the compact protocol, including class- and sample-wise explained variances (top), mean robust loadings as line graphs, mean robust scores as panels of points (bottom). Polygons around loadings and bars around scores represent 1 standard deviation. A legend with main mode position and explained variance of each endmember. Classes span from 0.19-1784 µm. For further reading see Dietze and Dietze (2019).

10 Supplement link, data availability

https://doi.pangaea.de/10.1594/PANGAEA.906582

11 Author contribution

GS carried out the sediment sampling and measured various sediment properties. GS also prepared the manuscript with contributions from all co-authors. KH, BW, and BD designed the study. WD carried out the magnetic measurements, AWR carried out the fossil counting and interpretation, JP was in charge of the lipid biomarker measuring program.

12 Competing interests

The authors declare that they have no conflict of interest.

13 Acknowledgements

This study was funded by the Federal Ministry of Education and Research of Germany (BMBF) as part of the CAME II project (Central Asia: Climatic Tipping Points & Their Consequences), project number 03G0863D and 03G0863E. T. Ehlers, M. Schaller, J. Starke, A. Koutsodendris, and E. Dietze are thanked for helping at various stages of the study.

References

Aichner, B., Herzschuh, U., Wilkes, H., Vieth, A., and Böhner, J.: δD values of n-alkanes in Tibetan lake sediments and aquatic macrophytes - A surface sediment study and application to a 16 ka record from Lake Koucha, Organic Geochemistry, 41 (8), 779-790, doi.org/10.1016/j.orggeochem.2010.05.010, 2010.

Aitchison, J.: Relative variation diagrams for describing patterns of compositional variability, Mathematical Geology, 22 (4), 487-511, doi.org/10.1007/BF00890330, 1990.

Balco, G. and Rovey II, C.W.: Isochron method for cosmogenic-nuclide dating of buried soils and sediments, Am. J. Sci.308, 1083-1114, doi.org/10.2475/10.2008.02, 2008.

Berke, M. A.: Reconstructing Terrestrial Paleoenvironments Using Sedimentary Organic Biomarkers, in: Methods in Paleoecology, Vertebrate Paleobiology and Paleoanthropology, edited by: Croft D., Su D., Simpson S., Springer, Cham, 121-149, 2018.

Borchers, B., Marrero, S., Balco, G., Caffee, M., Goehring, B., Lifton, N., Nishiizumi, K., Phillips, F., Schaefer, J., and Stone, J.: Geological calibration of spallation production rates in the CRONUS-Earth project, Quaternary Geochronology 31, 188-198, doi.org/10.1016/j.quageo.2015.01.009, 2016.

Becken, M., Hölz, S., Fiedler-Volmer, R., Hartmann, K., Wünnemann, B., and Burkhardt, H.: Electrical resistivity image of the Jingsutu Graben at the NE margin of the Ejina Basin (NW China) and implications for the basin development, Geophysical Research Letters, 34 (9), L09315, doi:10.1029/2007GL029412, 2007.

Blair, T. C. and McPherson, J. G.: Alluvial fan processes and forms, in: Geomorphology of desert environments, edited by: Abrahams A.A., Parsons A.J., Springer, Dordrecht, 354-402, 1994.

Boogaart, van den K. G., and Tolosana-Delgado, R. (Eds.): Analyzing compositional data with R., Heidelberg-New York-Dodrecht-London, Springer, 273 pp., doi.org/10.1007/978-3-642-36809-7, 2013.

Braucher, R., Merchel, S., Borgomano, J., and Bourlès, D.L.: Production of cosmogenic radionuclides at great depth: A multi element approach, Earth and Planetary Science Letters 309, 1-9, doi:10.1016/j.epsl.2011.06.036, 2011.

Chadima, M. and Hrouda, F.: Remasoft 3.0 a user-friendly paleomagnetic data browser and analyzer, Travaux Géophysiques, 27, 20-21, 2006.

Che, X. and Li, G.: Binary sources of loess on the Chinese Loess Plateau revealed by U-Pb ages of zircon, Quaternary Research, 80 (3), 545-551, 2013.

Chen, F. H., Yu, Z. C., Yang, M. L., Ito, E., Wang, S. M., Madsen, D. B., Huang, X. Z., Zhao, Y., Sato, T., Birks, H. J. B., Bommer, I., Chen, J. H., An, C. B., and Wünnemann, B.: Holocene moisture evolution in arid central Asia and its out-of phase relationship with Asian monsoon history, Quaternary Science Reviews, 27, 351-364, 2008.

Chmeleff, J., von Blanckenburg, F., Kossert, K., and Jakob, D.: Determination of the 10Be half-life by multicollector ICP-MS and liquid scintillation counting, Nuclear Instruments and Methods in Physics Research Section B: Beam Interactions with Materials and Atoms 268, 192-199, doi.org/10.1016/j.nimb.2009.09.012, 2010.

Clark, P. U., Archer, D., Pollard, D., Blum, J. D., Rial, J. A., Brovkin, V., Mix, A. C., Pisias, N. G., and Roy, M.: The middle Pleistocene transition: Characteristics, mechanisms, and implications for long-term changes in atmospheric pCO2, Quaternary Science Reviews, 25 (23-24), 3150-3184, doi.org/10.1016/j.quascirev.2006.07.008, 2006.

Cohen, K. M. and Gibbard, P. L.: Global chronostratigraphical correlation table for the last 2.7 million years, version 2019 QI-500, Quaternary International, 500, 20-31, 2019.

Cunningham, W. D., Windley, B. F., Dorjnamjaa, D., Badamgarov, J., and Saandar, M.: Late Cenozoic transpression in southwestern Mongolia and the Gobi Altai-Tien Shan connection, Earth and Planetary Science Letters, 140, 67-81, 1996.

Derbyshire, E., Meng, X. M., and Kemp, R. A.: Provenance, transport and characteristics of modern aeolian dust in western Gansu Province, China, and interpretation of the Quaternary loess record, J. Arid Environ. 39, 497-516, 1998.

Diekmann, B. and Kuhn, G.: Sedimentary record of the mid-Pleistocene climate transition in the southeastern South Atlantic (ODP Site 1090), Palaeogeography, Palaeoclimatology, Palaeoecology, 182 (3-4), 241-258, 2002.

Dietze, E., Hartmann, K., Diekmann, B., Ijmker, J., Lehmkuhl, F., Opitz, S., et al.: An end-member algorithm for deciphering modern detrital processes from lake sediments of Lake Donggi Cona, NE Tibetan Plateau, China, Sedimentary Geology, 243-244, 169-180, doi.org/10.1016/j.sedgeo.2011.09.014, 2012.

Dietze, E. and Dietze, M.: Grain-size distribution unmixing using the R package EMMAgeo, E&G Quaternary Sci. J., 68, 29-46, doi.org/10.5194/egqsj-68-29-2019, 2019.

Dill, H. G.: Residual clay deposits on basement rocks: The impact of climate and the geological setting on supergene argillitization in the Bohemian Massif (Central Europe) and across the globe, Earth-Science Reviews, 165, 1-58, 2017.

Eglinton, T. I. and Eglinton, G.: Molecular proxies for paleoclimatology, Earth and Planetary Science Letters, 275 (1-2), 1-16, doi. org/10.1016/j.epsl.2008.07.012, 2008.

Ficken, K. J., Li, B., Swain, D. L., and Eglinton, G.: An n-alkane proxy for the sedimentary input of submerged/floating freshwater aquatic macrophytes, Organic geochemistry, 31 (7-8), 745-749, 2000.

Gat, J. R.: Oxygen and hydrogen isotopes in the hydrological cycle, Annual Review of Earth and Planetary Sciences, 24 (1), 225-262, doi.org/10.1146/annurev.earth.24.1.225, 1996.

Gingele, F. X., De Deckker, P., and Hillenbrand, C. D.: Clay mineral distribution in surface sediments between Indonesia and NW Australia - source and transport by ocean currents, Marine Geology, 179 (3-4), 135-146, 2001.

Granger, D. E.: Cosmogenic Nuclide Burial Dating in Archaeology and Paleoanthropology, Treatise on Geochemistry 14, 81-97, 2014.

Guo, Z. T., Ruddiman, W. F., Hao, Q. Z., Wu, H. B., Qiao, Y. S., Zhu, R. X., Peng, S. Z., Wei, J. J., Yuan, B. Y., and Liu, T. S.: Onset of Asian desertification by 22 Myr ago inferred from loess deposits in China, Nature, 416 (6877), 159-163, 2002.

Hartmann, K. and Wünnemann, B.: Hydrological changes and Holocene climate variations in NW China, inferred from lake sediments of Juyanze palaeolake by factor analyses, Quaternary International, 194, 28-44, 2009.

Hartmann, K., Wünnemann, B., Hölz, S., Hrätschell, A., and Zhang, H. C.: Neotectonic constraints on Ejina inland basin in north-central China, derived from remote sensing, geomorphology and geophysical analyses, in: Growth and Collapse of the Tibetan Plateau, edited by: Gloaguen, R., Ratschbacher, L., Geological Society, London, Special Publications, 353, 221-233, 2011.

Head, M. J. and Gibbard, P. L.: Early-Middle Pleistocene transitions: Linking terrestrial and marine realms, Quaternary International, 389, 7-46, doi.org/10.1016/j.quaint.2015.09.042, 2015.

Herb, C., Zhang, W., Koutsodendris, A., Appel, E., Fang, X., and Pross, J.: Environmental implications of the magnetic record in Pleistocene lacustrine sediments of the Qaidam Basin, NE Tibetan Plateau, Quaternary international, 313, 218-229, 2013.

Herb, C., Koutsodendris, A., Zhang, W., Appel, E., Fang, X., Voigt, S., and Pross, J.: Late Plio-Pleistocene humidity fluctuations in the western Qaidam Basin (NE Tibetan Plateau) revealed by an integrated magnetic - palynological record from lacustrine sediments, Quaternary Research, 84 (3), 457-466, 2015.

https://doi.org/10.5194/se-2019-163
Preprint. Discussion started: 4 November 2019

Hetzel, R., Niedermann, S., Tao, M., Kubik, P. W., Ivy-Ochs, S., Gao, B., and Strecker, M. R.: Low slip rates and long-term preservation of geomorphic features in Central Asia, Nature, 417 (6887), 428-432, 2002.

Hillier, S.: Erosion, sedimentation, and sedimentary origin of clays, in: Velde, B. (Ed.), Clays and the environment. Springer Verlag, Berlin, 162-219, 1995.

Hillier, S.: Quantitative analysis of clay and other minerals in sandstones by X-ray powder diffraction (XRPD), International Association of Sedimentologist Special Publication, 34, 213-251, 2003.

Hölz, S., Polag, D., Becken, M., Fiedler-Volmer, R., Zhang, H. C., Hartmann, K., and Burkhardt, H.: Electromagnetic and geoelectric investigation of the Gurinai structure, Inner Mongolia, NW China, Tectonophysics, 445 (1-2), 26-48, 2007.

Hu, F. and Yang, X.: Geochemical and geomorphological evidence for the provenance of aeolian deposits in the Badain Jaran Desert, northwestern China, Quaternary Science Reviews, 131, 179-192, 2016.

Huang, Y. S., Schuman, B., Wang, Y., and Webb, T.: Hydrogen isotope ratios of individual lipids in lake sediments as novel tracers of climatic and environmental change: A surface sediment test, Journal of Paleolimnology, 31 (3), 363-375, doi.org/10.1023/B:JOPL.0000021855.80535.13, 2004.

Jeong, G. Y.: Bulk and single-particle mineralogy of Asian dust and a comparison with its source soils, J. Geophys. Res., 113, D02208, doi:10.1029/2007JD008606, 2008.

Kirschvink, J.L.: The least-squares line and plane and the analysis of palaeomagnetic data, Geophys. J. Int., 62, 699-718, 1980.

Korschinek, G., Bergmaier, A., Faestermann, T., Gerstmann, U.C., Knie, K., Rugel, G., Wallner, A., Dillmann, I., Dollinger, G., von Gostomski, C.L., Kossert, K., Maiti, M., Poutivtsev, M., and Remmert, A.: A new value for the half-life of 10Be by Heavy-Ion Elastic Recoil Detection and liquid scintillation counting, Nuclear Instruments and Methods in Physics Research Section B: Beam Interactions with Materials and Atoms 268, 187-191, doi.org/10.1016/j.nimb.2009.09.020, 2010.

Koutsodendris, A., Sachse, D., Appel, E., Herb, C., Fischer, T., Fang, X., and Pross, J.: Prolonged monsoonal moisture availability preconditioned glaciation of the Tibetan Plateau during the Mid-Pleistocene Transition, Geophysical Research Letters, 45, 13,020-13,030, doi.org/10.1029/2018GL079303, 2018.

Kukla, G.: Loess stratigraphy in central China, Quaternary Science Reviews, 6, 191-219, 1987.

Li, G., Pettke, T., and Chen, J.: Increasing Nd isotopic ratio of Asian dust indicates progressive uplift of the north Tibetan Plateau since the middle Miocene, Geology, 39 (3), 199-202, 2011.

Li, G., She, L., Jin, M., Yang, H., Madsen, D., Chun, X., ... and Chen, F.: The spatial extent of the East Asian summer monsoon in arid NW China during the Holocene and Last Interglaciation, Global and planetary change, 169, 48-65, doi.org/10.1016/j.gloplacha.2018.07.008, 2018.

Li, G., Madsen, D. B., Jin, M., Stevens, T., Tao, S., She, L., Yang, L., Li, F, Wei, H., Duan, Y., and Chen, F.: Orbital scale lake evolution in the Ejina Basin, central Gobi Desert, China revealed by K-feldspar luminescence dating of paleolake shoreline features Quaternary International, 482, 109-121, 2018b.

https://doi.org/10.5194/se-2019-163
Preprint. Discussion started: 4 November 2019

Solid Earth Discussions
Open Access
EGU

Li, X., Cheng, G., Ge, Y., Li, H., Han, F., Hu, X., … and Cai, X.: Hydrological cycle in the Heihe River Basin and its implication for water resource management in endorheic basins, Journal of Geophysical Research: Atmospheres, 123, 890.914, doi.org/10.1002/2017JD027889, 2018.

Li, Y., Yang, J., Tan, L., and Duan, F.: Impact of tectonics on alluvial landforms in the Hexi Corridor, Northwest China, Geomorphology, 28 (3-4), 299-308, 1999.

Li, Z., Sun, D., Chen, F., Wang, F., Zhang, Y., Guo, F., Wang, X., and Li, B.: Chronology and paleoenvironmental records of a drill core in the central Tengger Desert of China, Quaternary Science Reviews, 85, 85-98, 2014.

Lifton, N., Sato, T., and Dunai, T. J.: Scaling in situ cosmogenic nuclide production rates using analytical approximations to atmospheric cosmic-ray fluxes, Earth and Planetary Science Letters 386: 149-160, doi.org/10.1016/j.epsl.2013.10.052, 2014.

Liu, X., Yu, J., Wang, P., Zhang, Y., and Du, C.: Lake evaporation in a hyper-arid environment, Northwest of China - measurement and estimation, Water, 8 (11), 527, doi:10.3390/w8110527, 2016.

Long, H. and Shen, J.: Underestimated 14C-based chronology of late Pleistocene high lake-level events over the Tibetan Plateau and adjacent areas: Evidence from the Qaidam Basin and Tengger Desert, Science China Earth Sciences, 58, 183-194, doi.org/10.1007/s11430-014-4993-2, 2015.

Lü, Y., Gu, Z., Aldahan, A., Zhang, H., Possnert, G., and Lei, G.: 10 Be in quartz gravel from the Gobi Desert and evolutionary history of alluvial sedimentation in the Ejina Basin, Inner Mongolia, China, Chinese Science Bulletin, 55 (33), 3802-3809, 2010.

Marrero, S.M., Phillips, F.M., Borchers, B., Lifton, N., Aumer, R., and Balco, G.: Cosmogenic nuclide systematics and the CRONUScalc program, Quaternary Geochronology 31, 160-187, doi.org/10.1016/j.quageo.2015.09.005, 2016.

Métivier, F., Gaudemer, Y., Tapponnier, P., and Klein, M.: Mass accumulation rates in Asia during the Cenozoic, Geophysical Journal International, 137 (2), 280-318, 1999.

Mischke, S.: Mid and Late Holocene palaeoenvironment of the lakes Eastern Juyanze and Sogo Nur in NW China, based on ostracod species assemblages and shell chemistry, Berliner geowiss. Abh., E 35, 131 p., 2001.

Mölg, T., Maussion, F., and Scherer, D.: Mid-Latitude Westerlies as a Driver of Glacier Variability in Monsoonal High Asia, Nature Climate Change, 4, 68-73, 10.1038/nclimate2055, 2014.

Nishiizumi, K.: Preparation of 26Al AMS standards, Nuclear Instruments and Methods Part B 223-224, 388-392, 2004.

Nishiizumi, K., Imamura, M., Caffee, M.W., Southon, J.R., Finkel, R.C., and McAninch, J.: Absolute calibration of 10Be AMS standards, Nuclear Instruments and Methods in Physics Research Section B: Beam Interactions with Materials and Atoms 258, 403-413, 2007.

Norris, T.L., Gancarz, A.J., Rokop, D.J., and Thomas, K.W.: Half-life of 26Al, Lunar Planet. Sci. Conf., J. Geophys. Res. 88, B331, 1983.

Pan, B., Chen, D., Hu, X., Cao, X., Chen, J., and Mao, J.: Drainage evolution of the Heihe River in western Hexi Corridor, China, derived from sedimentary and magnetostratigraphic results, Quaternary Science Reviews, 150, 250-263, 2016.

https://doi.org/10.5194/se-2019-163
Preprint. Discussion started: 4 November 2019

Pang, J., Yu, J., Zheng, D., Wang, W., Ma, Y., Wang, Y., ... and Wang, Y.: Neogene expansion of the Qilian Shan, north Tibet: Implications for the dynamic evolution of the Tibetan Plateau, Tectonics, 38, 1018-1032, doi.org/10.1029/2018TC005258, 2019.

Petschick, R., Kuhn, G., and Gingele, F.: Clay mineral distribution in surface sediments of the South Atlantic: sources, transport, and relation to oceanography, Marine Geology, 130 (3-4), 203-229, 1996.

Porter, S. C.: Loess records / China. W: Elias, S. (ed.), The Encyclopedia of Quaternary Sciences, Elsevier, Amsterdam, 1429-1440, 2007.

Prokopenko, A. A., Hinnov, L. A., Williams, D. F., and Kuzmin, M. I.: Orbital forcing of continental climate during the Pleistocene: A complete astronomically tuned climatic record from Lake Baikal, SE Siberia, Quaternary Science Reviews, 25 (23-24), 3431-3457, doi.org/10.1016/j.quascirev.2006.10.002, 2006.

Raymo, M. E., Lisiecki, L. E., and Nisancioglu, K. H.: Plio-Pleistocene ice volume, Antarctic climate, and the global δ18O record. Science, 313 (5786), 492-495, doi.org/10.1126/science.1123296, 2006.

Rudersdorf, A., Hartmann, K., Yu, K., Stauch, G., and Reicherter, K.: Seismites as indicators for Holocene seismicity in the northeastern Ejina Basin, Inner Mongolia, Geological Society, London, Special Publications, 432 (1), 213-231, 2017.

Sachse, D., Billault, I., Bowen, G. J., Chikaraishi, Y., Dawson, T. E., Feakins, S. J., et al.: Molecular paleohydrology: Interpreting the hydrogen-isotopic composition of lipid biomarkers from photosynthesizing organisms. Annual Review of Earth and Planetary Sciences, 40 (1), 221-249, doi.org/10.1146/annurev-earth-042711-105535, 2012.

Schaller, M., Ehlers, T. A., Stor, T., Torrent, J., Lobato, L., Christl, M., and Vockenhuber, C.: Timing of European fluvial terrace formation and incision rates constrained by cosmogenic nuclide dating, Earth and Planetary Science Letters, 451, 221-231, 2016.

Schimpf, S.: Herkunft und Ablagerungsmilieu quartärer Sedimente im Einzugsgebiet des Heihe, NW China, (engl.: Sources and depositional environment of Quaternary sediments in the Heihe catchment, NW China), Dissertation submitted to the Faculty of Mathematics and Natural Sciences, University Potsdam, 195 p. [in German], 2019.

Shang, Y., Kaakinen, A., Beets, C. J., and Prins, M. A.: Aeolian silt transport processes as fingerprinted by dynamic image analysis of the grain size and shape characteristics of Chinese loess and Red Clay deposits, Sedimentary geology, 375, 36-48, 2018.

SI, supplementary information: doi.pangaea.de/10.1594/PANGAEA.906582

Singer, A.: The paleoclimatic interpretation of clay minerals in sediments - a review, Earth-Science Reviews, 21, 251-293, 1984.

Singer, B. S.: A Quaternary geomagnetic instability time scale, Quaternary Geochronology, 21, 29-52, 2014.

Song, Y., Fang, X., Torii, M., Ishikawa, N., Li, J., and An, Z.: Late Neogene rock magnetic record of climatic variation from Chinese eolian sediments related to uplift of the Tibetan Plateau, J. Asian Earth Sci. 30, 324-332, 2007.

Song, S., Niu, Y., Zhang, L., Wei, C., Liou, J. G., and Su, L.: Tectonic evolution of early Paleozoic HP metamorphic rocks in the North Qilian Mountains, NW China: new perspectives, Journal of Asian Earth Sciences, 35 (3-4), 334-353, 2009.

https://doi.org/10.5194/se-2019-163
Preprint. Discussion started: 4 November 2019

Su, Q., Nie, J., Luo, Z., Li, M., Heermance, R., and Garzione, C.: Detection of strong precession cycles from the late Pliocene sedimentary records of northeastern Tibetan Plateau, Geochemistry, Geophysics, Geosystems, 20, 3901-3912, doi.org/10.1029/2019GC008447, 2019.

Sun, J.: Provenance of loess material and formation of loess deposits on the Chinese Loess Plateau. Earth and Planetary Science Letters, 203 (3-4), 845-859, 2002.

Sun, Y. and An, Z.: Late Pliocene-Pleistocene changes in mass accumulation rates of eolian deposits on the central Chinese Loess Plateau, Journal of Geophysical Research: Atmospheres, 110 (D23), 2005.

Sun, Y., An, Z., Clemens, S. C., Bloemendal, J., and Vandenberghe, J.: Seven million years of wind and precipitation variability on the Chinese Loess Plateau, Earth and Planetary Science Letters, 297 (3-4), 525-535, doi.org/10.1016/j.epsl.2010.07.004, 2010.

Tjallingii, R., Röhl, U., Kölling, M., and Bickert, T.: Influence of the water content on X-ray fluorescence core-scanning measurements in soft marine sediments, Geochemistry, Geophysics, Geosystems, 8 (2), Q02004, doi:10.1029/2006GC001393, 2007.

Verbrugge, L. N., Schipper, A. M., Huijbregts, M. A., Van der Velde, G., and Leuven, R. S.: Sensitivity of native and non-native mollusc species to changing river water temperature and salinity, Biological Invasions, 14 (6), 1187-1199, 2012.

Wang, G.X. and Cheng, G.D.: Water resource development and its influence on the environment in arid areas of China - the case of the Hei River Basin, J. Arid Environ. 43, 121-131, 1999.

Wang, N., Li, Z., Cheng, H., Li, Y., and Huang, Y.: High lake levels on Alxa Plateau during the Late Quaternary, Chinese science bulletin, 56 (17), 1799-1808, 2011.

Wang, F., Sun, D., Chen, F., Bloemendal, J., Guo, F., Li, Z., Zhang, Y., Li, B., and Wang, X.: Formation and evolution of the Badain Jaran Desert, North China, as revealed by a drill core from the desert centre and by geological survey, Palaeogeography, Palaeoclimatology, Palaeoecology, 426, 139-158, 2015.

Wang, W., Zheng, W., Zhang, P., Li, Q., Kirby, E., Yuan, D., ... and Pang, J.: Expansion of the Tibetan Plateau during the Neogene, Nature communications, 8, 15887, DOI: 10.1038/ncomms15887, 2017.

Weltje, G. J. and Tjallingii, R.: Calibration of XRF core scanners for quantitative geochemical logging of sediment cores: theory and application, Earth and Planetary Science Letters, 274 (3-4), 423-438, 2008.

Weltje, G. J., Bloemsma, M. R., Tjallingii, R., Heslop, D., Röhl, U., and Croudace, I. W.: Prediction of geochemical composition from XRF core scanner data: a new multivariate approach including automatic selection of calibration samples and quantification of uncertainties, in: Micro-XRF Studies of Sediment Cores. Springer, Dordrecht, 507-534, 2015.

Willenbring, J. K. and von Blanckenburg, F.: Long-term stability of global erosion rates and weathering during late-Cenozoic cooling, Nature, 465 (7295), 211-214, doi:10.1038/nature09044, 2010.

Wilson, M. J.: The origin and formation of clay minerals in soils: past, present and future perspectives, Clay Minerals 34 (1), 7-25, 1999.

Wünnemann, B. and Hartmann, K.: Morphodynamics and Paleohydrography of the Ejina Basin, Inner Mongolia, China, Zeitschrift für Geomorphologie, N.F., Suppl.-Bd. 126, 147-168, 2002.

Wünnemann, B., Hartmann, K., Altmann, N., Hambach, U., Pachur, H. J., and Zhang, H.: 22. Interglacial and glacial fingerprints from lake deposits in the Gobi Desert, NW China, in: Developments in Quaternary Sciences (7), Elsevier, 323-347, 2007.

Wünnemann, B., Hartmann, K., Janssen, M., and Hucai, C. Z.: Responses of Chinese desert lakes to climate instability during the past 45,000 years, in: Developments in Quaternary Sciences, Vol. 9: Late Quaternary Climate Change and Human Adaptation in Arid China, edited by D.B. Madsen, F. Chen, X. Gao, ISSN 1571-0866, 11-23, DOI:10.1016/S1571-0866(07)09003-3, 2007b.

Yan, D.: Interplay between Lake and Catchment Processes in Kuhai Lake Basin, NE Tibetan Plateau, China during Late Holocene. Dissertation, Freie Universität Berlin, Department of Earth Sciences, 151 pp., 2017.

Yang, X., Ma, N., Dong, J., Zhu, B., Xu, B., Ma, Z., and Liu, J.: Recharge to the interdune lakes and Holocene climatic changes in the Badain Jaran Desert, western China, Quaternary Research 73, 10-19, 2010.

Yang, X., Scuderi, L., Paillou, P., Liu, Z., Li, H., and Ren, X.: Quaternary environmental changes in the drylands of China - a critical review, Quaternary Science Reviews, 30 (23-24), 3219-3233, 2011.

Yang, X., Li, H., and Conacher, A.: Large-scale controls on the development of sand seas in northern China, Quaternary International, 250, 74-83, 2012.

Yu, K., Hartmann, K., Nottebaum, V., Stauch, G., Lu, H., Zeeden, C., Yi, S., Wünnemann, B., and Lehmkuhl, F.: Discriminating sediment archives and sedimentary processes in the arid endorheic Ejina Basin, NW China using a robust geochemical approach, Journal of Asian Earth Sciences, 119, 128-144, 2016.

Zhang, H. C., Ming, Q. Z., Lei, G. L., Zhang, W. X., Fan, H. F., Chang, F. Q., Wünnemann, B., and Hartmann, K.: Dilemma of dating on lacustrine deposits in a hyperarid inland basin of NW China, Radiocarbon, 48 (2), 219-226, 2006.

Zhu, B., Yu, J., Rioual, P., Gao, Y., Zhang, Y., and Min, L.: Geomorphoclimatic characteristics and landform information in the Ejina Basin, Northwest China, Environmental Earth Sciences, 73 (11), 7547-7560, 2015.

Zheng, D., Wang, W., Wan, J., Yuan, D., Liu, C., Zheng, W., Zhang, H., Pang, J., and Zhang, P.: Progressive northward growth of the northern Qilian Shan-Hexi Corridor (northeastern Tibet) during the Cenozoic, Lithosphere, 9 (3), 408-416, 2017.

Zhisheng, A., Clemens, S. C., Shen, J., Qiang, X., Jin, Z., Sun, Y., … and Lu, F.: Glacial-Interglacial Indian Summer Monsoon Dynamics, Science, 333 (6043), 719-723, doi.org/10.1126/science.1203752, 2011.

https://doi.org/10.5194/se-2019-163
Preprint. Discussion started: 4 November 2019

Solid Earth Discussions
Open Access

Table 1: Information for burial ages from drill core GN200

Sample	Lab ID	Grain size µm	Depth m	$^{26}Al/^{10}Be$ ratio	Burial age[1] Ma
GN200 19a	GN6	125-500	19.1 ± 0.1	2.12 ± 0.15	2.12 ± 0.15
GN200 21a	GN7	125-500	20.3 ± 0.1	1.74 ± 0.11	2.52 ± 0.07
GN200 34b	GN8	125-500	53.1 ± 0.1	3.97 ± 0.37	0.84 ± 0.12
GN200 68 a[2]	GN1	125-250	129.2 ± 0.3	2.42 ± 0.70	1.86 ± 0.43
GN200 102a[2]	GN2	250-500	217.6 ± 0.1	2.61 ± 0.53	1.70 ± 0.13
GN200 102a[2]	GN3	125-250	217.6 ± 0.1	4.73 ± 1.05	0.48 ± 0.21

[1] Calculated simple burial age based concentrations in Table 2.
[2] Sample with ratios close to blank and high errors. Interpretation of burial age with caution.

https://doi.org/10.5194/se-2019-163
Preprint. Discussion started: 4 November 2019

Solid Earth
Discussions
Open Access

Table 2: Analytical information for burial age calculations

Sample	Lab ID	$m_{(qtz)}$	^{27}Al Conc.	^{26}Al/^{27}Al$^{(1)}$	Error	^{26}Al Conc. (corr)$^{(2)}$	^{9}Be$^{(3)}$	^{10}Be/^{9}Be$^{(4)}$	Error	^{10}Be Conc. (corr)$^{(5)}$
		g	ppm		%	10^3 atoms/$g_{(qtz)}$	mg		%	10^3 atoms/$g_{(qtz)}$
GN200 19a	GN6	22.34	78	1.28E-13	5.4	221.96 ± 12.01	0.3307	1.07E-13	4.4	104.79 ± 4.68
GN200 21a	GN7	75.24	94	6.82E-14	5.4	143.02 ± 7.78	0.3298	2.81E-13	3.7	82.00 ± 3.03
GN200 34b	GN8	93.55	123	2.05E-14	7.3	56.17 ± 4.12	0.3283	6.15E-14	5.4	14.16 ± 0.79
GN200 68 a$^{(6)}$	GN1	47.14	117	3.40E-15	26.0	8.89 ± 2.31	0.3284	8.60E-15	9.6	3.67 ± 0.45
GN200 102a$^{(6)}$	GN2	12.86	119	2.19E-14	17.0	58.14 ± 9.87	0.3287	1.38E-14	10.0	22.27 ± 2.51
GN200 102a$^{(6)}$	GN3	19.78	121	1.33E-14	16.8	36.08 ± 6.04	0.3278	7.60E-15	11.1	7.63 ± 1.10

$^{(1)}$ ^{26}Al/^{27}Al ratios measured against KN01-5-3 and KN01-4-3 (Nishiizumi, 2004).

$^{(2)}$ No correction for a ^{26}Al chemistry blank.

$^{(3)}$ Phenakite carrier of GFZ Potsdam.

$^{(4)}$ ^{10}Be/^{9Be} ratios measured against KN01-6-2 and KN01-5-3 (Nishiizumi et al., 2007).

$^{(5)}$ Corrected for a ^{10}Be chemistry blank of (1.98 ±0.59) x 10^4 atoms.

$^{(6)}$ Sample with ratios close to blank level and high errors. Interpretation of burial ages with caution.

https://doi.org/10.5194/se-2019-163
Preprint. Discussion started: 4 November 2019

Solid Earth
Discussions
Open Access
EGU

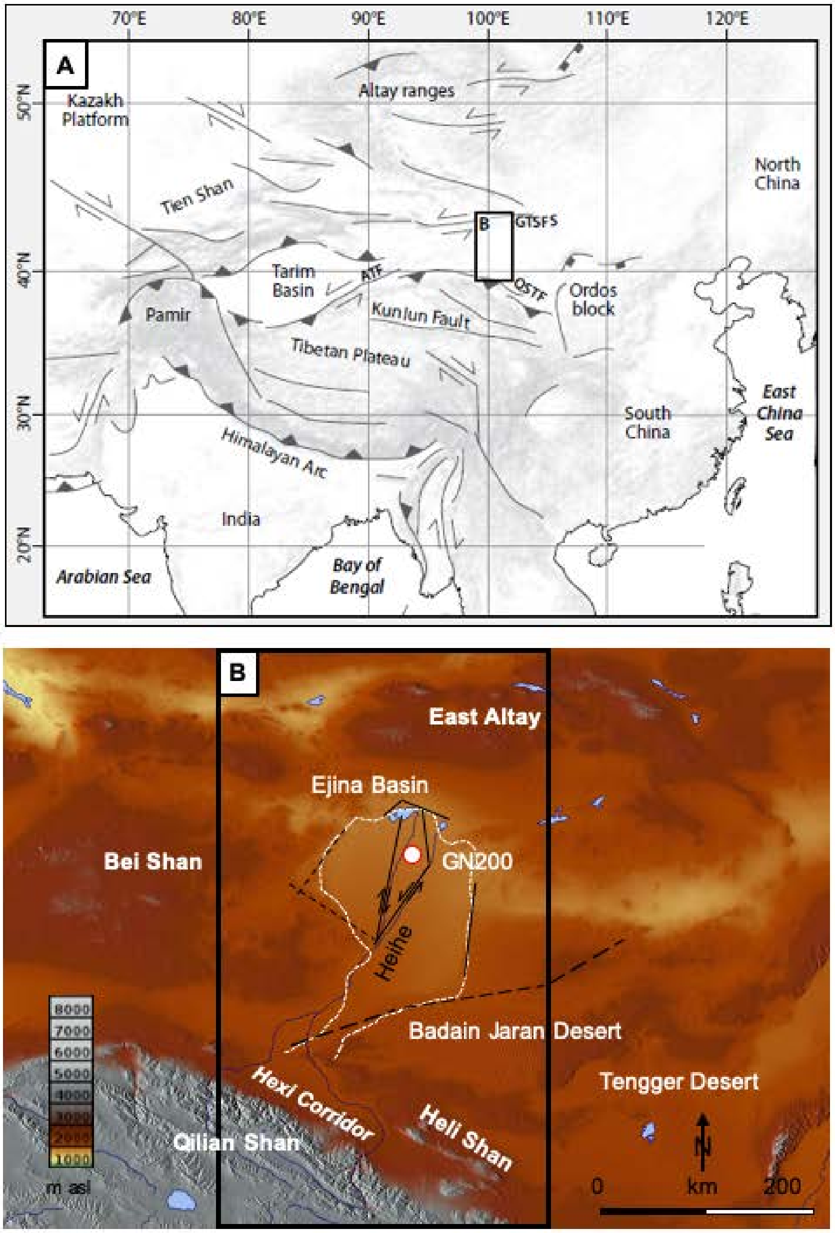

Fig. 1

https://doi.org/10.5194/se-2019-163
Preprint. Discussion started: 4 November 2019

Solid Earth Discussions
Open Access
EGU

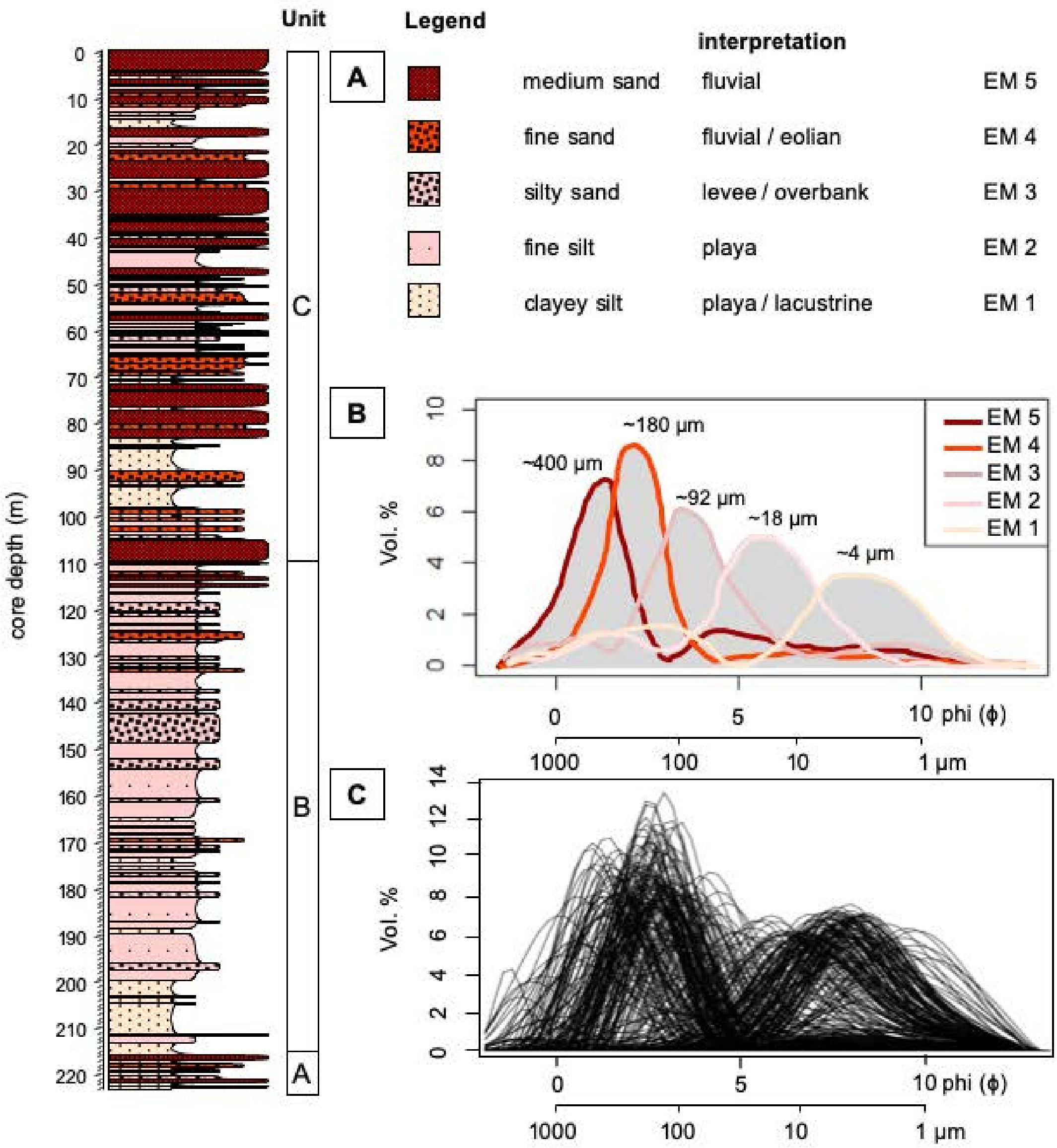

Fig. 2

https://doi.org/10.5194/se-2019-163
Preprint. Discussion started: 4 November 2019

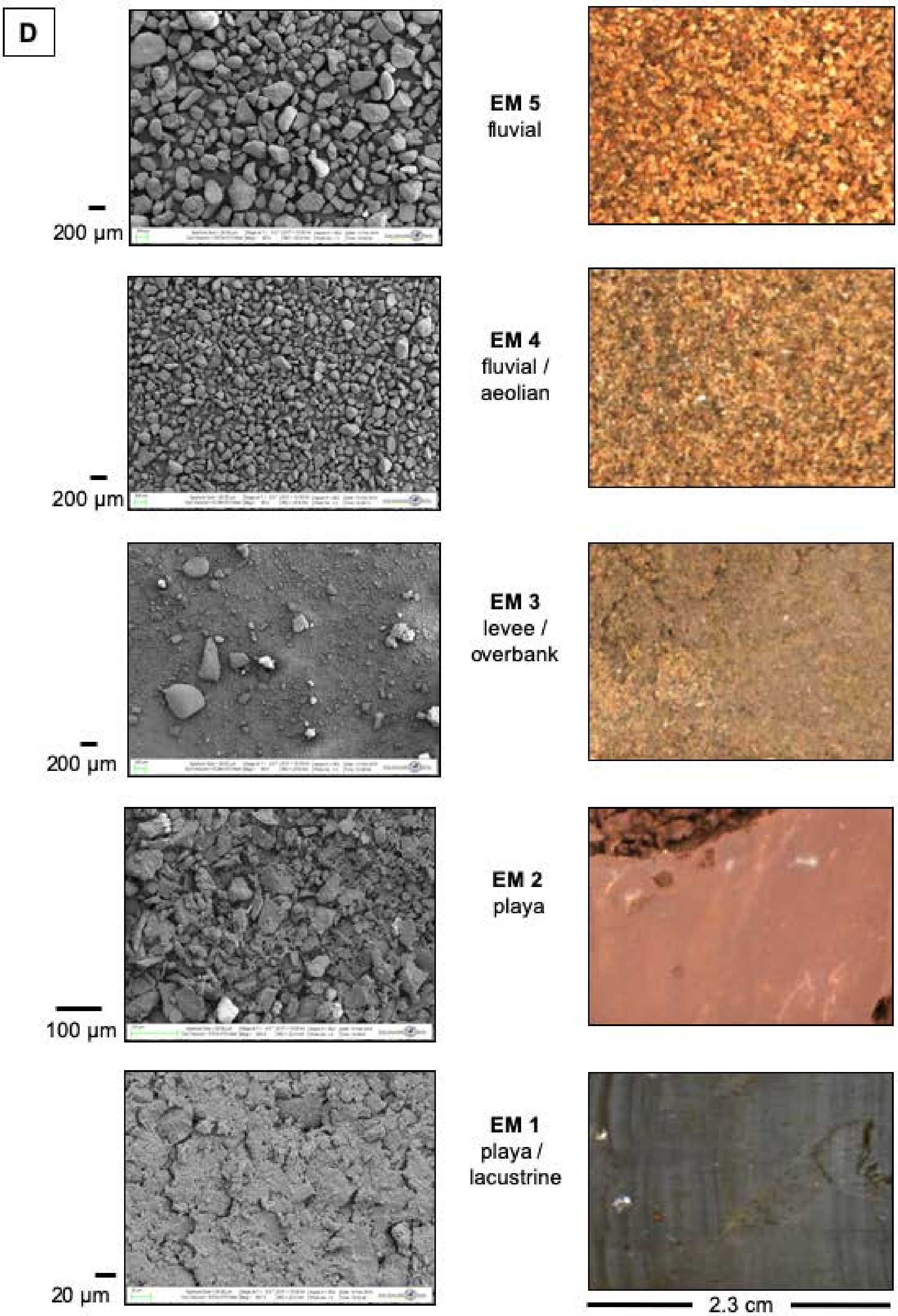

Fig. 2 ctd.

https://doi.org/10.5194/se-2019-163
Preprint. Discussion started: 4 November 2019

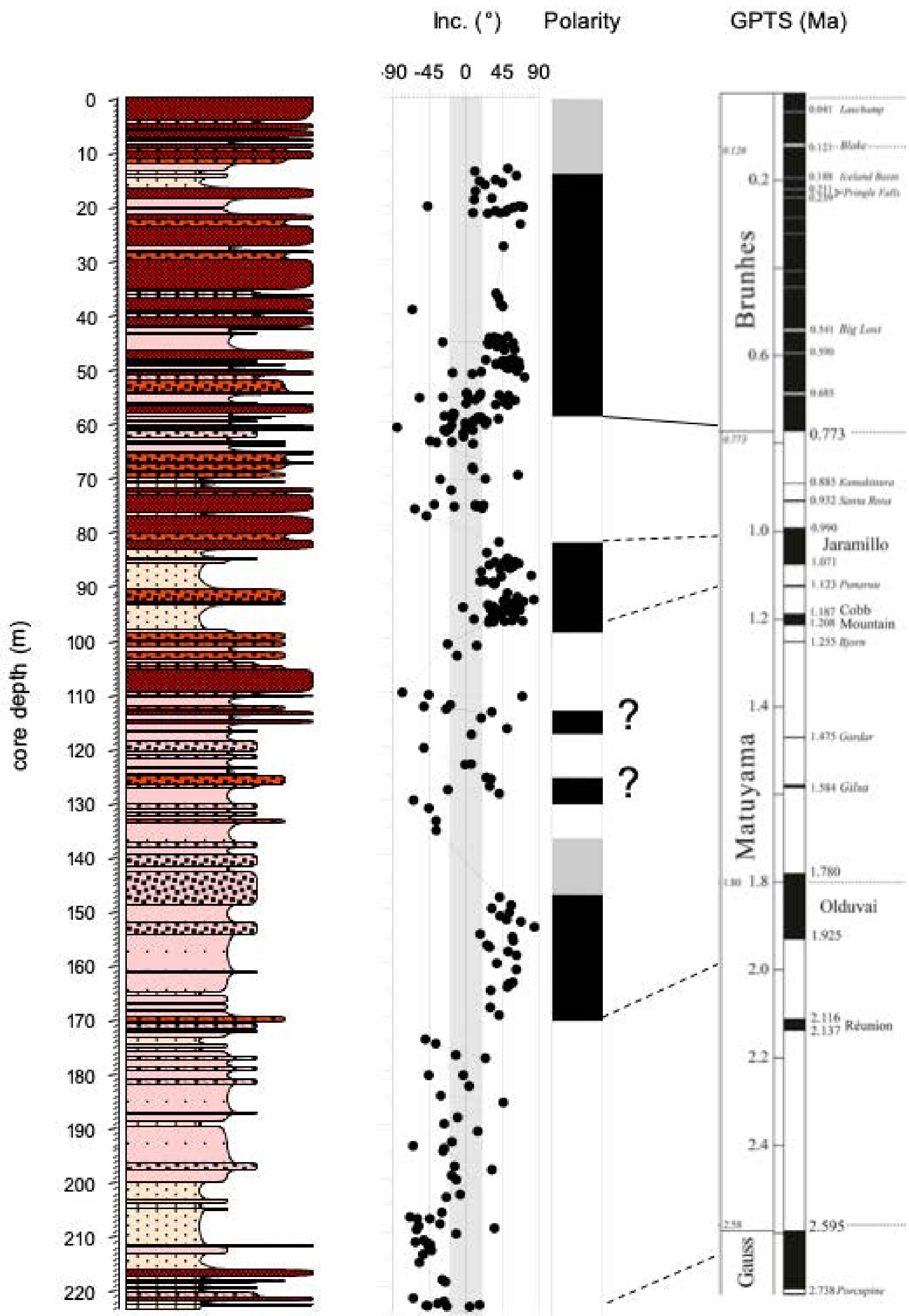

Fig. 3

https://doi.org/10.5194/se-2019-163
Preprint. Discussion started: 4 November 2019

Solid Earth Discussions
Open Access
EGU

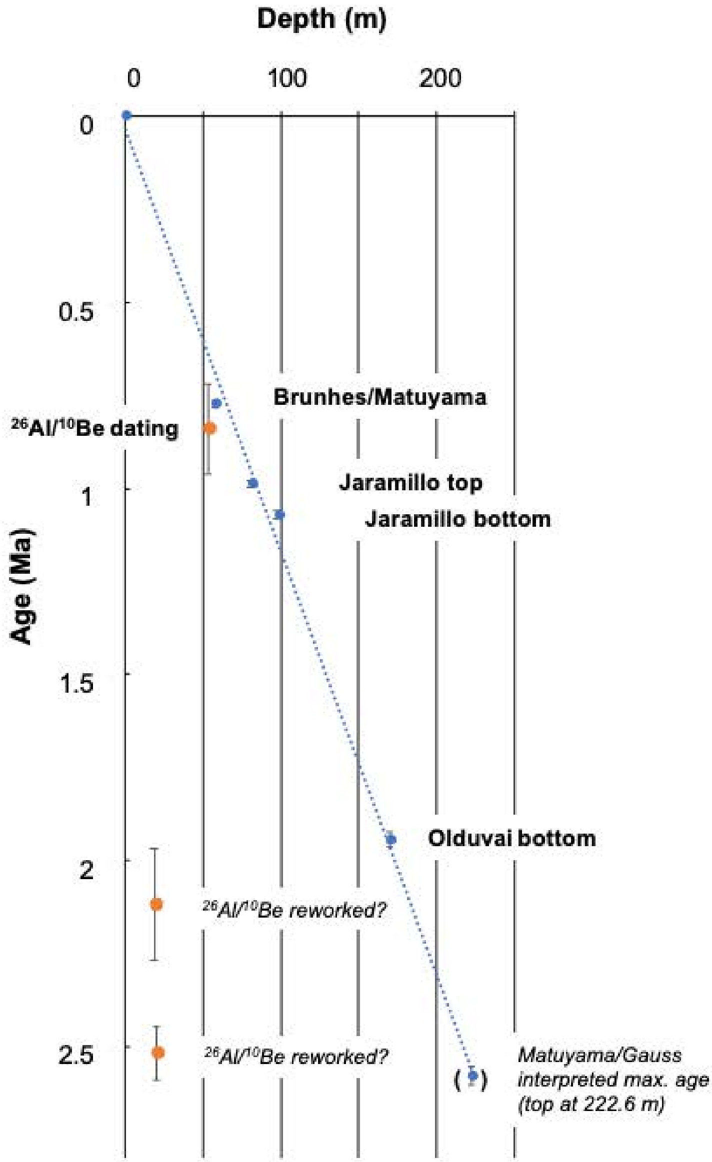

Fig. 4

https://doi.org/10.5194/se-2019-163
Preprint. Discussion started: 4 November 2019

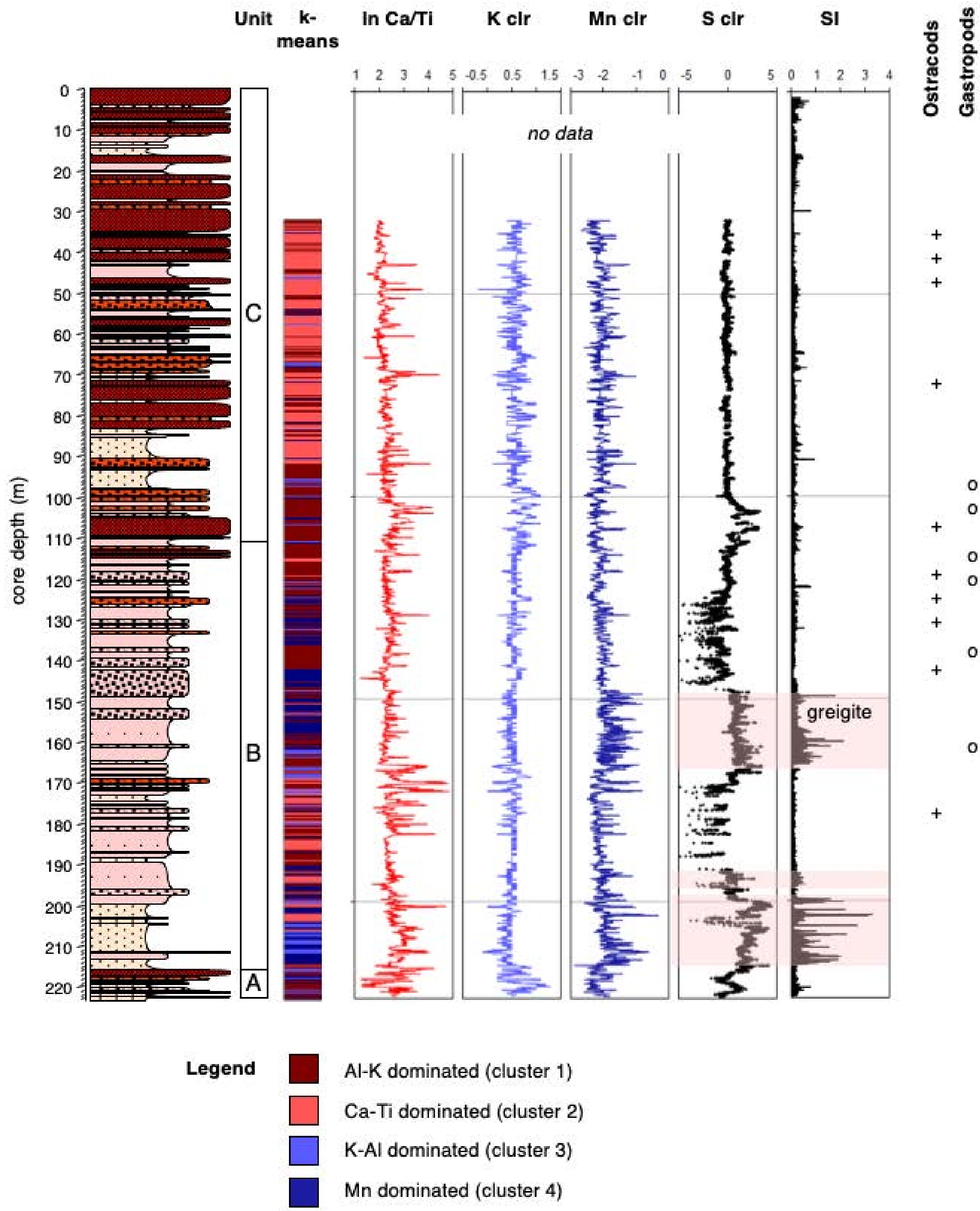

Fig. 5

https://doi.org/10.5194/se-2019-163
Preprint. Discussion started: 4 November 2019

Solid Earth
Discussions
Open Access

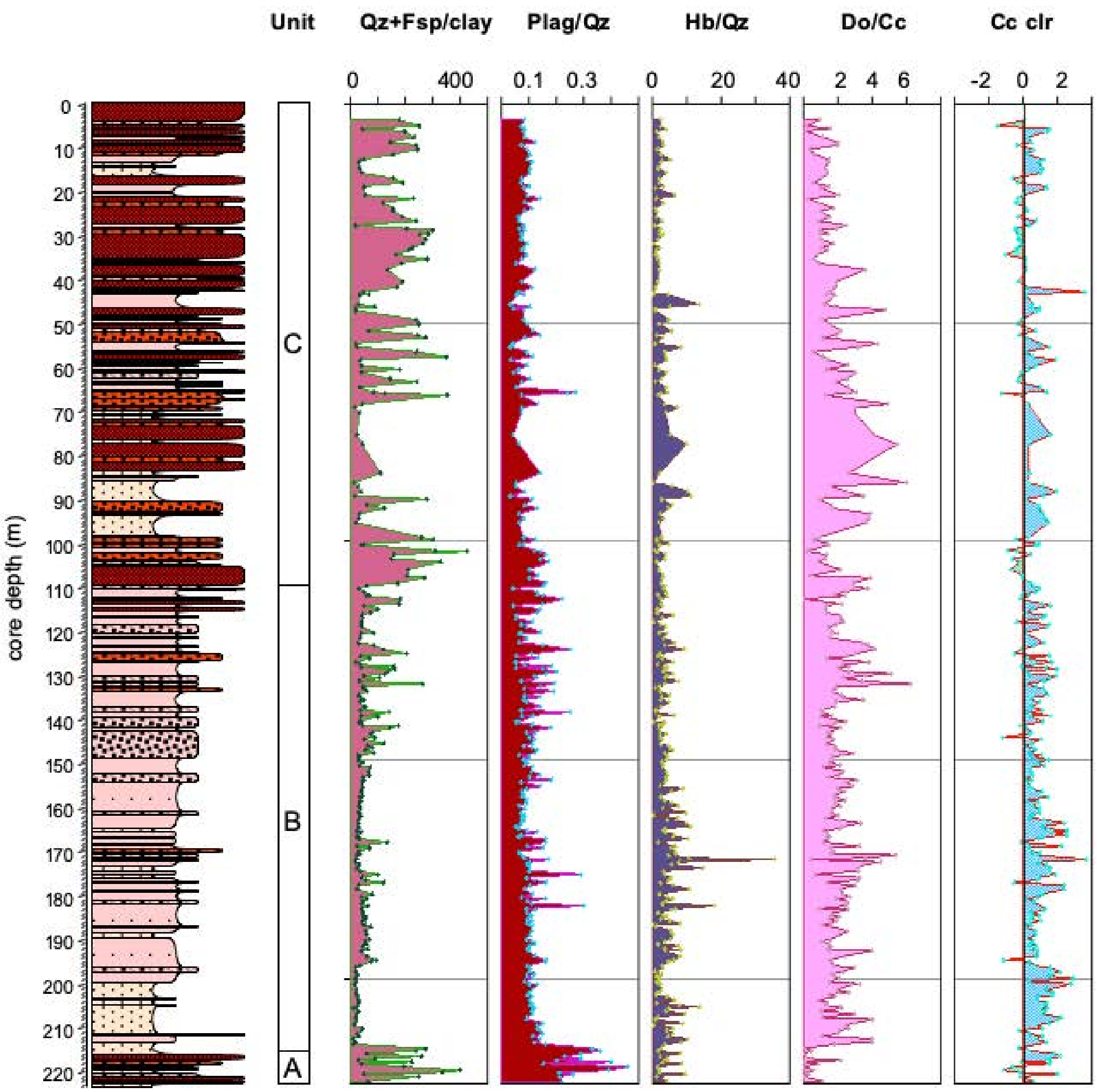

Fig. 6

https://doi.org/10.5194/se-2019-163
Preprint. Discussion started: 4 November 2019

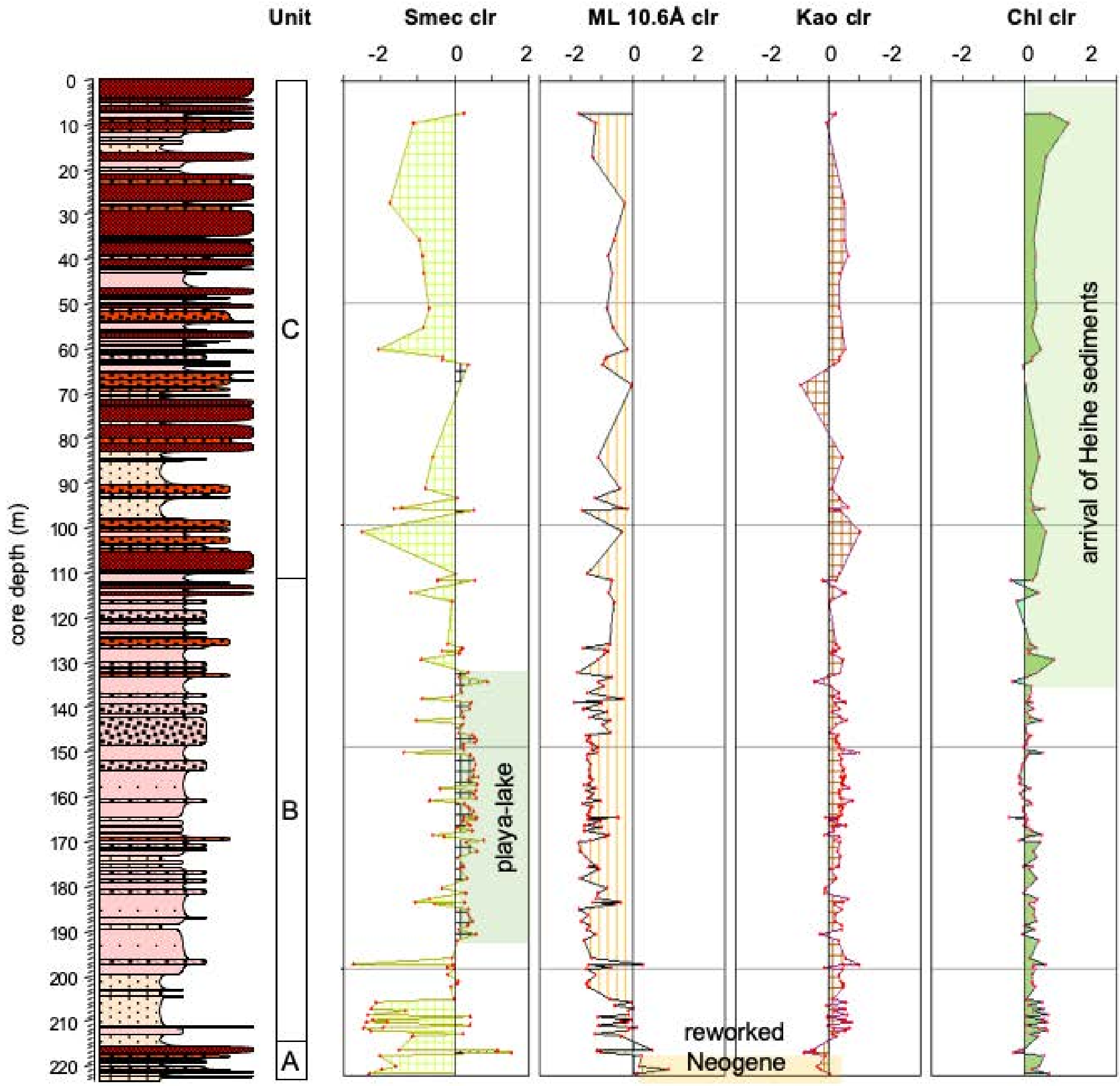

Fig. 7

https://doi.org/10.5194/se-2019-163
Preprint. Discussion started: 4 November 2019

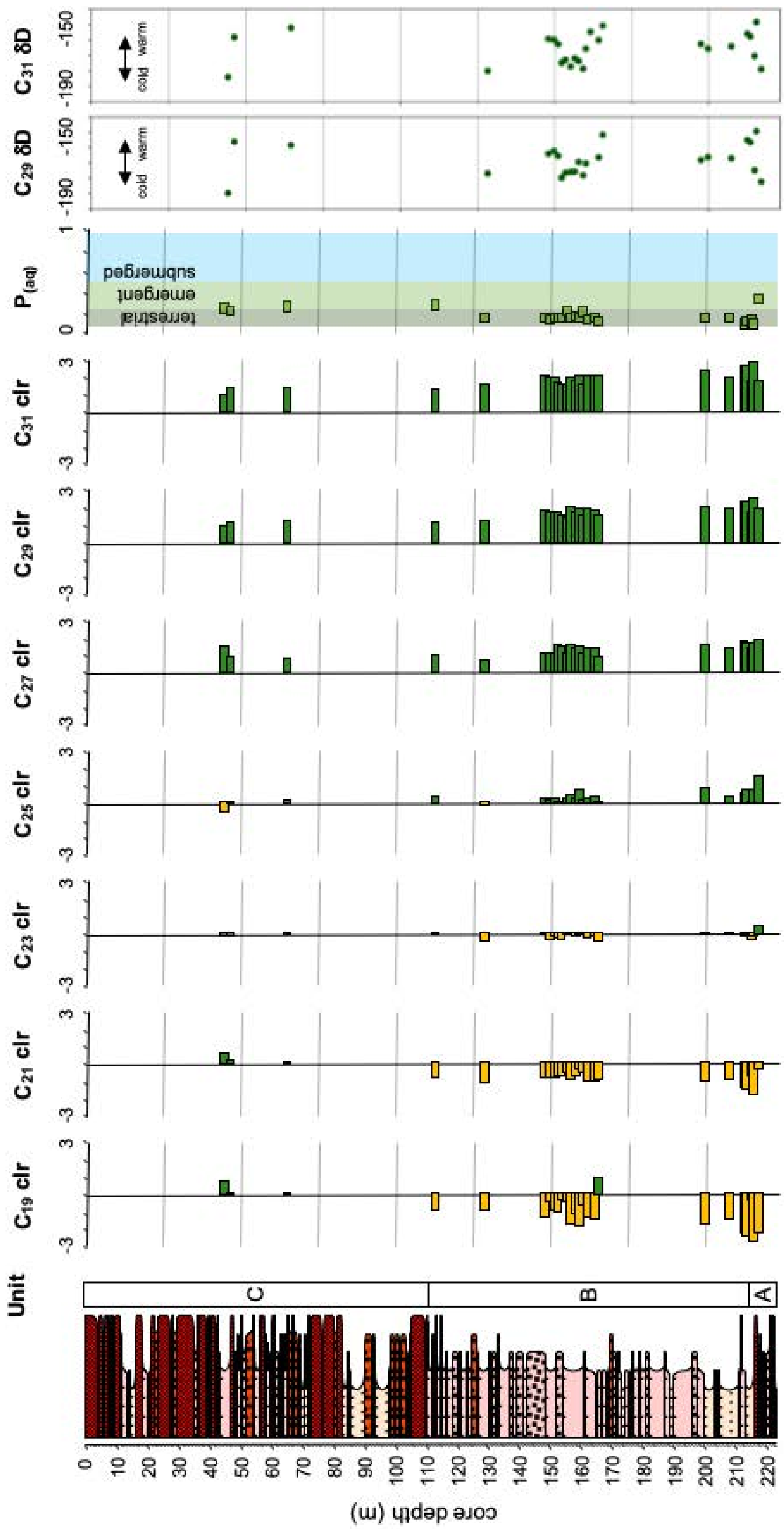

Fig. 8

https://doi.org/10.5194/se-2019-163
Preprint. Discussion started: 4 November 2019

Solid Earth
Discussions
Open Access
EGU

Fig. 9

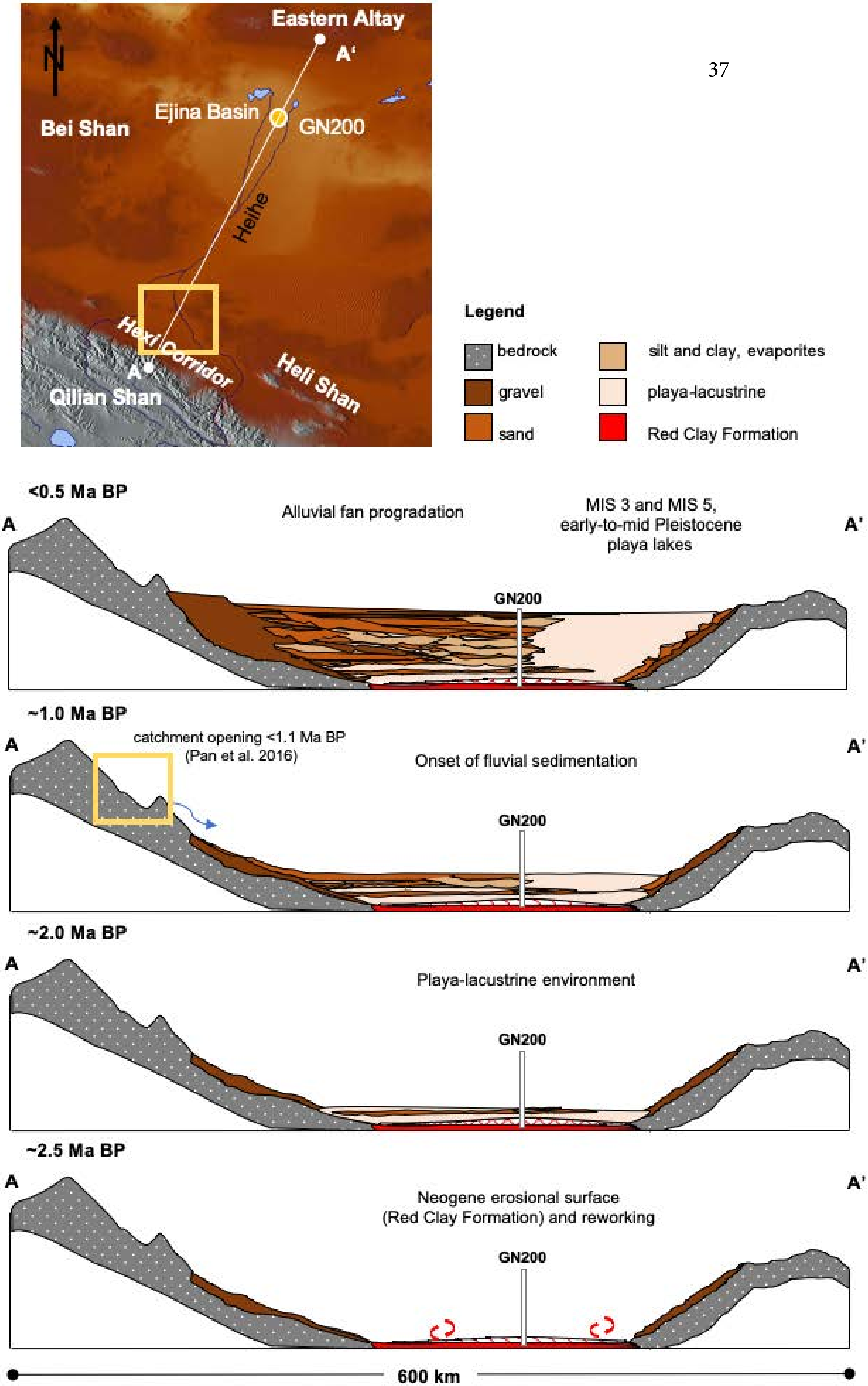

https://doi.org/10.5194/se-2019-163
Preprint. Discussion started: 4 November 2019

Solid Earth Discussions
Open Access
EGU

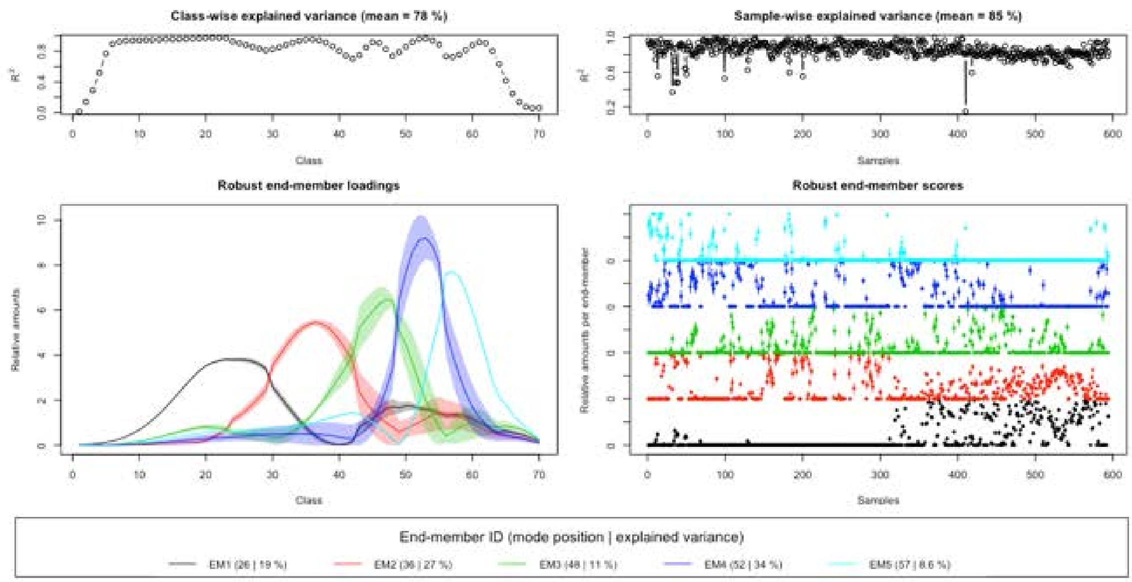

Appendix 1